



Large-scale proteomic analysis of Alzheimer's disease brain and cerebrospinal fluid reveals early changes in energy metabolism associated with microglia and astrocyte activation

Erik C. B. Johnson ^{1,2,22}✉, Eric B. Dammer ^{1,3,22}, Duc M. Duong^{1,3}, Lingyan Ping^{1,2,3}, Maotian Zhou^{1,2,3}, Luming Yin³, Lenora A. Higginbotham², Andrew Guajardo⁴, Bartholomew White⁴, Juan C. Troncoso⁴, Madhav Thambisetty⁵, Thomas J. Montine⁶, Edward B. Lee ⁷, John Q. Trojanowski ⁷, Thomas G. Beach⁸, Eric M. Reiman ⁹, Vahram Haroutunian ^{10,11}, Minghui Wang¹², Eric Schadt ¹², Bin Zhang¹², Dennis W. Dickson ¹³, Nilüfer Ertekin-Taner^{13,14}, Todd E. Golde¹⁵, Vladislav A. Petyuk¹⁶, Philip L. De Jager ¹⁷, David A. Bennett¹⁸, Thomas S. Wingo ^{1,2,19}, Srikanth Rangaraju ², Ihab Hajjar², Joshua M. Shulman^{20,21}, James J. Lah^{1,2}, Allan I. Levey ^{1,2}✉ and Nicholas T. Seyfried ^{1,2,3}✉

Our understanding of Alzheimer's disease (AD) pathophysiology remains incomplete. Here we used quantitative mass spectrometry and coexpression network analysis to conduct the largest proteomic study thus far on AD. A protein network module linked to sugar metabolism emerged as one of the modules most significantly associated with AD pathology and cognitive impairment. This module was enriched in AD genetic risk factors and in microglia and astrocyte protein markers associated with an anti-inflammatory state, suggesting that the biological functions it represents serve a protective role in AD. Proteins from this module were elevated in cerebrospinal fluid in early stages of the disease. In this study of >2,000 brains and nearly 400 cerebrospinal fluid samples by quantitative proteomics, we identify proteins and biological processes in AD brains that may serve as therapeutic targets and fluid biomarkers for the disease.

AD is a leading cause of death worldwide, with increasing prevalence as global life expectancy increases¹. Although AD is currently defined on the basis of amyloid-β plaque and tau neurofibrillary tangle deposition within the neocortex², the biochemical and cellular changes in the brain that characterize the disease beyond amyloid-β and tau deposition remain incompletely understood. Protein coexpression analysis is a powerful tool to understand biological network, pathway and cell type changes in human tissue^{3,4}. Communities of coexpressed proteins can be linked to disease processes and the most strongly correlated proteins or

'hubs' within these coexpression modules are enriched in key drivers of disease pathogenesis^{5–10}. Therefore, targeting hubs within protein coexpression modules most related to disease biology is a promising approach for drug and biomarker development^{11–14}. Here we describe a multicenter consortium study in the Accelerating Medicine Partnership for AD (AMP-AD) to analyze more than 2,000 human brain tissues by quantitative mass spectrometry (MS)-based proteomics. We generate a consensus AD brain protein coexpression network, controlling for batch and other covariates, from 453 brains obtained from multiple research centers. We validate

¹Gozueta Alzheimer's Disease Research Center, Emory University School of Medicine, Atlanta, GA, USA. ²Department of Neurology, Emory University School of Medicine, Atlanta, GA, USA. ³Department of Biochemistry, Emory University School of Medicine, Atlanta, GA, USA. ⁴Johns Hopkins School of Medicine, Baltimore, MD, USA. ⁵Clinical and Translational Neuroscience Section, Laboratory of Behavioral Neuroscience, National Institute on Aging, National Institutes of Health, Bethesda, MD, USA. ⁶Department of Pathology, School of Medicine, Stanford University, Palo Alto, CA, USA. ⁷Center for Neurodegenerative Disease Research, Department of Pathology and Laboratory Medicine, Perelman School of Medicine at the University of Pennsylvania, Philadelphia, PA, USA. ⁸Department of Pathology, Banner Sun Health Research Institute, Sun City, AZ, USA. ⁹Banner Alzheimer's Institute, Arizona State University and University of Arizona, Phoenix, AZ, USA. ¹⁰Departments of Psychiatry and Neuroscience, Icahn School of Medicine at Mount Sinai, New York, NY, USA. ¹¹JJ Peters VA Medical Center MIRECC, Bronx, NY, USA. ¹²Department of Genetics and Genomic Sciences, Mount Sinai Center for Transformative Disease Modeling, Icahn School of Medicine at Mount Sinai, New York, NY, USA. ¹³Department of Neuroscience, Mayo Clinic, Jacksonville, FL, USA. ¹⁴Department of Neurology, Mayo Clinic, Jacksonville, FL, USA. ¹⁵Department of Neuroscience, Center for Translational Research in Neurodegenerative Disease, McKnight Brain Institute, University of Florida, Gainesville, FL, USA. ¹⁶Biological Sciences Division, Pacific Northwest National Laboratory, Richland, WA, USA. ¹⁷Center for Translational & Computational Neuroimmunology, Department of Neurology, Taub Institute, Columbia University Irving Medical Center, New York Presbyterian Hospital, New York, NY, USA. ¹⁸Rush Alzheimer's Disease Center, Rush University Medical Center, Chicago, IL, USA. ¹⁹Department of Human Genetics, Emory University School of Medicine, Atlanta, GA, USA. ²⁰Departments of Neurology, Neuroscience and Molecular & Human Genetics, Baylor College of Medicine, Houston, TX, USA. ²¹Jan and Dan Duncan Neurologic Research Institute, Texas Children's Hospital, Houston, TX, USA. ²²These authors contributed equally: Erik C.B. Johnson, Eric B. Dammer. ✉e-mail: erik.c.b.johnson@emory.edu; alevey@emory.edu; nseyfri@emory.edu

this protein network in a separate community-based cohort using a different MS-based technique for protein quantitation and show that the network is preserved in different brain regions affected in AD. By analyzing a separate cohort of normal aging brains, we are able to estimate the effect that aging has on the observed AD brain protein coexpression network. We also analyze disease specificity of the AD protein network changes by interrogating these changes in six other neurodegenerative diseases that encompass diverse brain pathologies, and validate observed changes by targeted protein measurements. One of the most strongly altered AD protein coexpression modules, which we term the ‘astrocyte/microglial metabolism’ module, is enriched in proteins linked to microglia, astrocytes and sugar metabolism and is enriched in protein products linked to AD genetic risk. Microglial protein markers within this module are biased toward an anti-inflammatory disease-associated state, suggesting that it reflects a protective or compensatory function in response to AD pathology. Proteins from this module are increased in cerebrospinal fluid in individuals with AD, including in the asymptomatic stage of the disease. Our results highlight the importance of inflammation, sugar metabolism, mitochondrial function, synaptic function, RNA-associated proteins and glia in the pathogenesis of AD and provide a robust framework for future proteomic and multiomic studies on AD brain and biofluid biomarkers.

Results

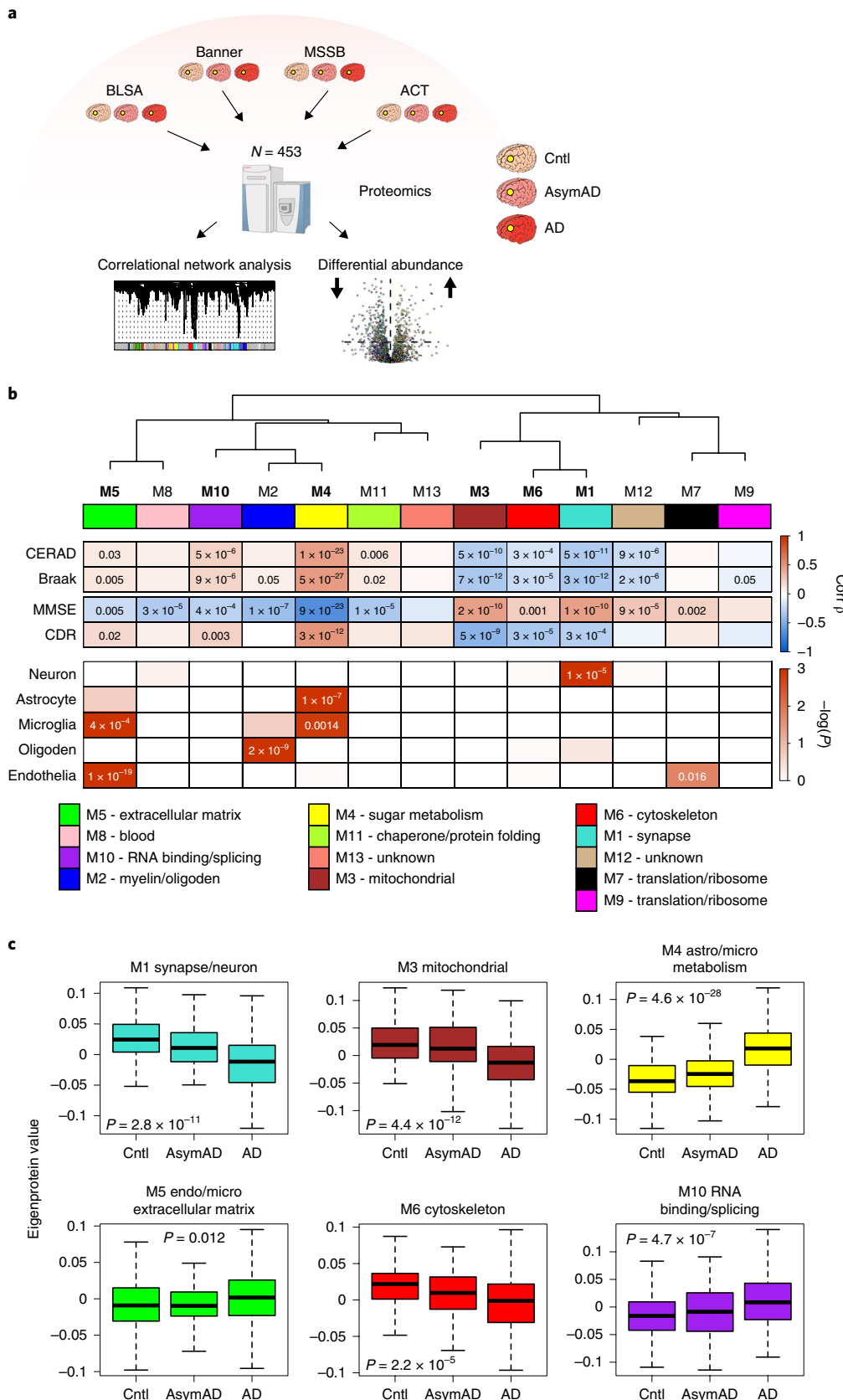
Construction and validation of a consensus AD protein coexpression network. We analyzed dorsolateral prefrontal cortex (DLPFC) tissue in 44 cases from the Baltimore Longitudinal Study of Aging (BLSA), 178 cases from the Banner Sun Health Research Institute (Banner), 166 cases from the Mount Sinai School of Medicine Brain Bank (MSSB) and 65 cases from the Adult Changes in Thought Study (ACT), for a total of 453 control, asymptomatic AD (AsymAD) and AD brains (Fig. 1a and Supplementary Table 1). AsymAD was defined as postmortem pathology consistent with an AD diagnosis but without dementia, based on the NIA research framework for AD². Tissues were analyzed by MS-based proteomics using label-free quantitation (LFQ) and the resulting MS data were processed using a common pipeline to arrive at 5,688 total quantified proteins. We included proteins with fewer than 50% missing values in subsequent analyses, as it was determined that this threshold was robust to potential spurious correlations given the power of the study (Extended Data Fig. 1). We also removed by regression the effects of age, sex and postmortem interval (PMI) on the protein quantitative data, even though these covariates did not strongly

influence data (Extended Data Fig. 2). The final adjusted 3,334 proteins were used to generate a protein coexpression network using the weighted correlation network analysis (WGCNA) algorithm. The resulting network consisted of 13 protein coexpression ‘modules’ or communities of proteins with similar expression patterns across the cases analyzed (Fig. 1b, Supplementary Figs. 1 and 2 and Supplementary Table 2). The modules ranged in size from 254 proteins (M1) to 20 proteins (M13). These modules could also be identified independently of the WGCNA algorithm using *t*-distributed stochastic neighbor embedding analysis (Extended Data Fig. 3), demonstrating that the protein communities identified by the WGCNA algorithm were robust. Gene ontology (GO) analysis of the protein module members revealed a clear ontology for 11 out of the 13 modules, encompassing a diverse mix of biological functions, processes and components (Fig. 1b and Supplementary Fig. 3). To assess whether a given coexpression module was related to AD, we correlated module eigenprotein—or first principal component (PC) of the module protein expression level—to neuropathological hallmarks of AD, amyloid- β plaques and neurofibrillary tangles. We also correlated module eigenproteins to cognitive function as assessed by the Mini-Mental Status Examination (MMSE) and functional status, as assessed by the Clinical Dementia Rating Scale (CDR), at the last research evaluations before death to capture module-disease relationships that may be independent of amyloid- β plaque or tau tangle pathology (Fig. 1b and Supplementary Fig. 1). We observed six modules that were significantly correlated with all pathological, cognitive and functional measures and whose ontologies could be best characterized by a structural component or biological process: modules M1 synapse, M3 mitochondrial, M4 glucose and carbohydrate metabolism (subsequently referred to as sugar metabolism), M5 extracellular matrix, M6 cytoskeleton and M10 RNA binding/splicing. The M4 sugar metabolism module showed the strongest AD trait correlations (cognition $r = -0.67$, $P = 8.5 \times 10^{-23}$; neurofibrillary tangle $r = 0.49$, $P = 4.7 \times 10^{-27}$; amyloid- β plaque $r = 0.46$, $P = 1.3 \times 10^{-23}$; and functional status $r = 0.52$, $P = 2.6 \times 10^{-12}$). Because AD neuropathology is not homogenous, even within the same brain region, and because neuropathological measurements of AD pathology are semiquantitative and subject to a certain degree of individual variability in assessment¹⁵, we also correlated module eigenproteins to MS measurements of amyloid- β and the tau microtubule binding region, which comprises neurofibrillary tangles, within the DLPFC tissue used for proteomic analysis (Extended Data Fig. 4). We observed strong concordance between neuropathological and molecular measurements of AD pathology.

Fig. 1 | Protein network analysis of asymptomatic and symptomatic AD brain. **a**, Protein levels in brain tissue from control (cntl), AsymAD and patients with AD ($N = 453$) were measured by label-free MS and analyzed by WGCNA and differential abundance. Brain tissue was analyzed from postmortem DLPFC (highlighted in yellow) in the BLSA ($n = 11$ control, $n = 13$ AsymAD, $n = 20$ AD, $n = 44$ total), Banner ($n = 26$ control, $n = 58$ AsymAD, $n = 94$ AD, $n = 178$ total), MSSB ($n = 46$ control, $n = 17$ AsymAD, $n = 103$ AD, $n = 166$ total) and ACT ($n = 11$ control, $n = 14$ AsymAD, $n = 40$ AD, $n = 65$ total). **b**, Protein correlation network consisting of 13 protein modules was generated from 3,334 proteins measured across four separate cohorts. Module eigenproteins, which represent the first PC of the protein expression within each module, were correlated with neuropathological hallmarks of AD (CERAD amyloid- β plaque score, where higher scores represent greater plaque burden and Braak, tau neurofibrillary tangle staging score, where higher scores represent greater extent of tangle burden), cognitive function (MMSE, where higher scores represent better cognitive function) and overall functional status (CDR, where higher scores represent worse functional status) (top). CERAD and Braak measures were from all cohorts, whereas MMSE was from Banner and CDR was from MSSB. Strength of positive (red) or negative (blue) correlation is shown by two-color heat map, with P values provided for all correlations with $P < 0.05$. Modules that showed a significant correlation with all four traits are highlighted in bold. The cell type nature of each protein module was assessed by module protein overlap with known neuron, astrocyte, microglia, oligodendrocyte (oligoden) and endothelia cell markers (middle). Significance of overlap is shown by one-color heat map, with P values provided for overlaps with $P < 0.05$. GO analysis of the proteins within each module clearly identified the biological processes associated with the module for most modules (bottom). **c**, Module eigenprotein level by case status for each protein module that had significant correlation to all four traits in **b**. Case status is from all cohorts (cntl, $n = 91$; AsymAD, $n = 98$; AD, $n = 230$ after network connectivity outlier removal). APOE genotype effects and other trait correlations for all modules are provided in Supplementary Fig. 1. Module eigenprotein correlations were performed using biweight midcorrelation and corrected by the Benjamini-Hochberg method. Protein module cell type overlap was performed using one-sided Fisher’s exact test with Benjamini-Hochberg correction. Differences in eigenprotein values were assessed by Kruskal-Wallis one-way analysis of variance (ANOVA). Box plots represent the median, 25th and 75th percentiles and whiskers represent measurements to the 5th and 95th percentiles.

Because many protein coexpression changes in the brain can be driven by cell type changes^{16,17}, we also assessed the cell type nature of each coexpression module by asking whether the module

was enriched in particular cell type marker proteins (Fig. 1b). We observed significant enrichment of neuronal proteins in the M1 synapse module and enrichment of oligodendrocyte markers in



the M2 myelin module, as expected. We also observed enrichment of astrocyte and microglial proteins in the M4 sugar metabolism module, microglial and endothelial proteins in the M5 extracellular matrix module and endothelial markers in the M7 translation/ribosome module. These findings suggest that the biological processes reflected by GO analysis for each module may be altered in AD within a particular cell type. To incorporate the cell type nature of each module into its description, we subsequently refer to those modules with strong cell type enrichment as the ‘M1 synapse/neuron’ module, the ‘M2 myelin/oligodendrocyte’ module, the ‘M4 astrocyte/microglial metabolism’ module and the ‘M5 endo/microextracellular matrix’ module.

To assess the relationship of the network modules to diagnostic classification, we measured the module eigenprotein values by case status (Fig. 1c and Supplementary Fig. 1). In general, most modules that were increased or decreased in AD compared to control also showed a trend or were significantly changed in the same direction in the AsymAD group, indicating that these modules reflect pathophysiological processes that begin early in the preclinical phase of AD. The M1 synapse/neuron, M3 mitochondrial and M4 astrocyte/microglial metabolism modules showed the strongest differences by case status. We also assessed the influence of APOE genotype on module eigenproteins, but did not find strong effects except for the APOE ε2 allele on the M2 myelin/oligodendrocyte module, which seemed to attenuate the observed changes in AD (Supplementary Fig. 1).

To validate the AD network, we analyzed 340 DLPFC brain tissues from a community-based aging cohort, the Religious Orders Study and Memory and Aging Project (ROS/MAP)^{18–20}, with a different MS-based protein quantification approach using isobaric multiplex tandem mass tags (TMTs)^{21–23}. A protein coexpression network was constructed from the ROS/MAP cases and network module preservation statistics as well as synthetic module eigenproteins were used to assess conservation of the consensus AD LFQ-based network in the ROS/MAP TMT-based network (Extended Data Fig. 5b,c and Supplementary Fig. 4). We found that all consensus LFQ modules were preserved in the ROS/MAP TMT-based network. Furthermore, targeted protein measurements in a cohort of 1,016 ROS/MAP control, AsymAD and AD brains by another MS protein quantification approach—selected reaction monitoring (SRM)—showed that individual module proteins had the same direction of change as the AD LFQ-based network coexpression module of which they were a member (Supplementary Figs. 5 and 6). In summary, we were able to construct a robust AD protein coexpression network from MS-based proteomic analysis of more than 450 human DLPFC brain tissues from multiple centers. We found that many of these modules correlated with AD neuropathology and cognitive function, reflected a number of different biological processes and cell types and were altered in the preclinical stage of AD.

The AD network is preserved in other brain regions. The consensus AD network was generated from analysis of DLPFC tissue.

To assess whether the network was similar in other brain regions commonly affected in AD, we analyzed control and AD brain tissue from the temporal cortex in a separate set of 111 brains from the Mayo Clinic and control, AsymAD and AD brain tissue from precuneus in the same set of brains from the BLSA (Fig. 2a) using LFQ-MS. Coexpression networks were built for each brain region and network preservation statistics were used to assess module preservation from DLPFC in temporal cortex (Fig. 2b) and precuneus (Fig. 2c). We found that all consensus AD network modules derived from DLPFC were preserved in temporal cortex and 12 out of the 13 modules were preserved in precuneus. Analysis of synthetic module eigenprotein values by case status showed similar differences between and among case groups in temporal cortex (Fig. 2d and Supplementary Fig. 7) and precuneus (Fig. 2e and Supplementary Fig. 8) brain regions, with changes in AsymAD more pronounced in precuneus than in DLPFC. These findings suggest that the consensus AD network is generalized across brain regions that are commonly affected in AD.

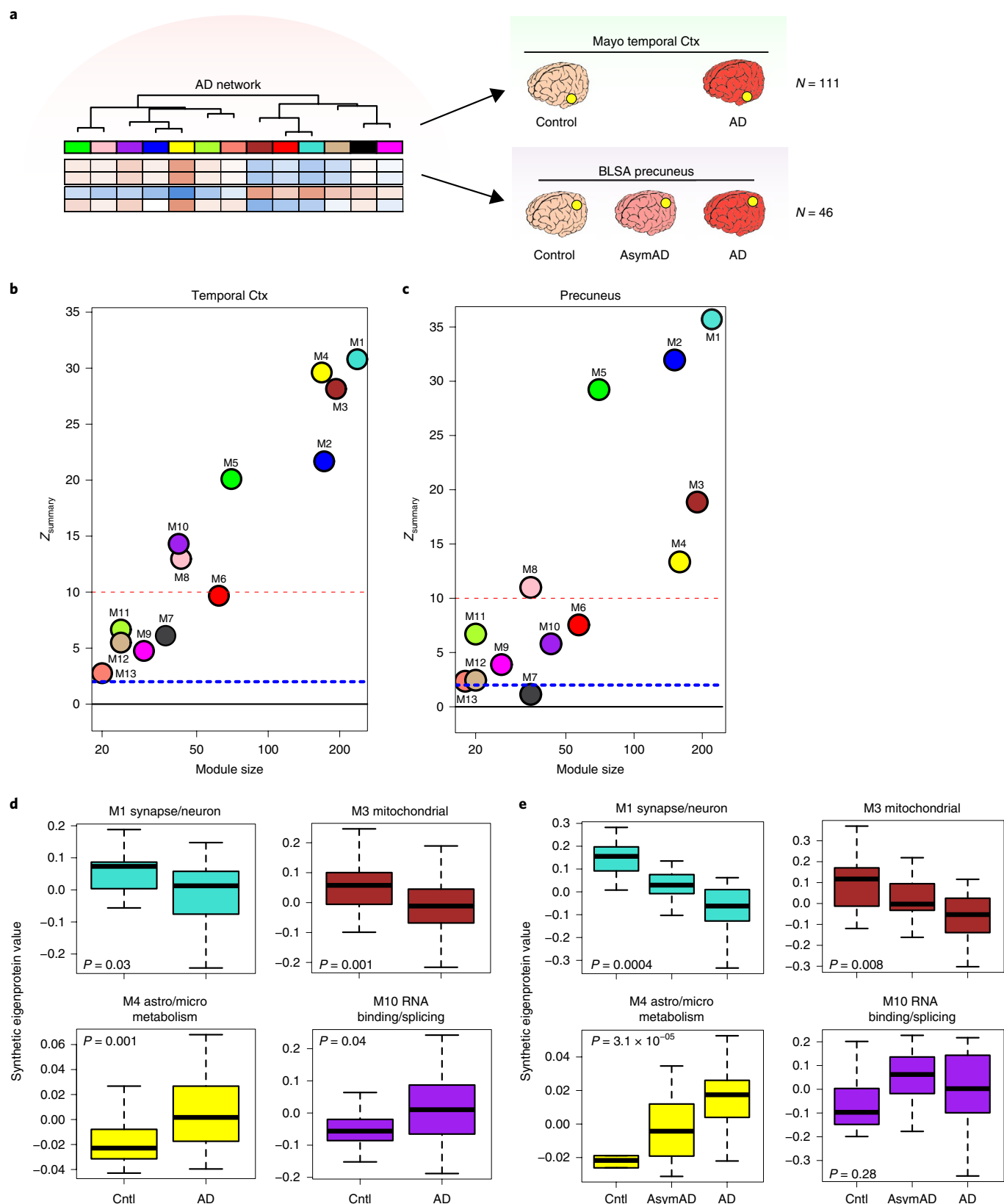
Effects of aging on AD network modules. To better understand the influence that aging—the strongest risk factor for AD—may have on the consensus AD network, we analyzed DLPFC tissues from Johns Hopkins in 84 individuals aged 30 to 69 years (Fig. 3a) by LFQ-MS. All individuals had a final primary neuropathological diagnosis of control. We created synthetic eigenproteins in the aging cohort from the consensus AD network modules and asked whether the synthetic module eigenproteins changed with age (Fig. 3b and Supplementary Fig. 9). We found that the M1 synapse/neuron and M4 astrocyte/microglial metabolism modules decreased and increased with aging, respectively, whereas the M3 mitochondrial and M10 RNA binding/splicing modules were not affected by aging. Other modules that appeared to be affected by aging included the M6 cytoskeleton, M7 translation/ribosome and M9 translation/ribosome modules (Supplementary Fig. 9). Additional information on the correlation of individual proteins with age and overlap with markers of cellular senescence is provided in Supplementary Table 3. These findings indicate that the relationship between aging and AD at the proteomic level is complex and that some, but not all, AD trait-associated modules are influenced by the aging process.

AD network changes in other neurodegenerative diseases. To explore the specificity of these network changes for AD, we analyzed 331 DLPFC tissues by LFQ-MS from control individuals and those with AD, amyotrophic lateral sclerosis (ALS), frontotemporal lobar degeneration with TDP-43 pathology (FTLD-TDP), progressive supranuclear palsy (PSP), corticobasal degeneration (CBD), Parkinson’s disease and Parkinson’s disease dementia (PD/PDD) and multiple systems atrophy (MSA) (Fig. 4a). We created synthetic eigenproteins for consensus AD network modules and assessed whether they changed in the different neurodegenerative diseases compared to AD (Fig. 4b, Supplementary Fig. 10 and

Fig. 2 | AD protein network is preserved in different brain regions. a–e, Preservation of AD protein network modules derived from analysis of DLPFC in other brain regions affected by AD. Protein levels in temporal cortex from a total of 111 control and AD cases (control, $n=28$; AD, $n=83$) from the Mayo Brain Bank and in precuneus from a total of 46 cases from the BLSA (control, $n=12$; AsymAD, $n=14$; AD, $n=20$) were measured by label-free MS and used to assess conservation of the AD brain protein network derived from DLPFC. Ctx, cortex (a). AD brain protein network preservation in temporal cortex (b) and precuneus (c). Module preservation was calculated using a composite z_{summary} score as described by Langfelder et al.⁵⁵ The dashed blue line indicates a z_{summary} score of 1.96 or false discovery rate (FDR) q value <0.05 , above which module preservation was considered statistically significant. The dashed red line indicates a z_{summary} score of 10 or FDR q value $\sim 1 \times 10^{-23}$, above which module preservation was considered highly statistically significant. Case status preservation in temporal cortex and precuneus (d,e). A synthetic eigenprotein was created for each AD network module as described in Extended Data Fig. 5 and measured by case status in temporal cortex (d) and precuneus (e). Asymptomatic AD was not assessed in the Mayo cohort and is therefore not included in the temporal cortex analyses. Synthetic eigenprotein analyses for modules M1, M3, M4 and M10 are shown. Analyses for all modules, with additional trait correlations, are provided in Supplementary Figs. 7 and 8. Differences in module synthetic eigenproteins by case status were assessed by two-sided Welch’s t -test (d) or Kruskal-Wallis one-way ANOVA (e). Box plots represent the median, 25th and 75th percentiles and whiskers represent measurements to the 5th and 95th percentiles.

Supplementary Table 4). We found that the M1 synapse/neuron and M4 astrocyte/microglial metabolism modules showed significant changes in FTLD-TDP and CBD cases, similarly to AD, whereas the M3 mitochondrial and M10 RNA binding/splicing modules showed more mixed changes across other diseases. To further validate these findings, we used a targeted MS method called parallel

reaction monitoring (PRM)²⁴ to measure 323 individual proteins from approximately one-third of the individuals analyzed in the untargeted experiments (Supplementary Fig. 11 and Supplementary Table 4). Protein levels across all cases were highly correlated ($r=0.92$, $P=1.4 \times 10^{-124}$) between LFQ and PRM measurements (Extended Data Fig. 6b). We created synthetic eigenproteins from



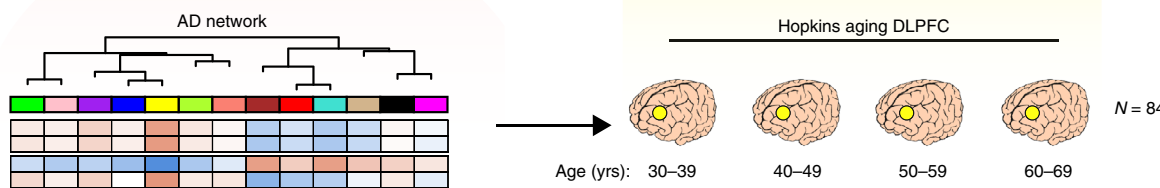
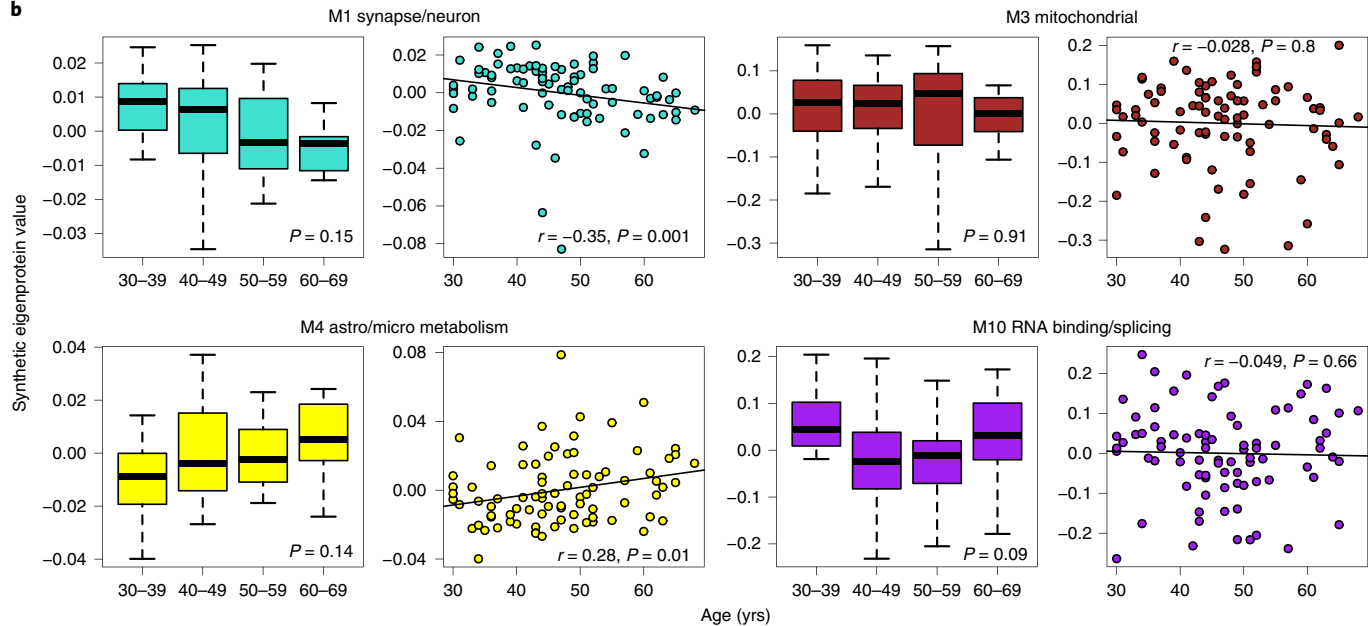
a**b**

Fig. 3 | Effects of aging on AD protein network modules. **a**, Protein levels were measured in DLPFC from cognitively healthy people who died at different ages (age 30–39 years, $n=20$; age 40–49 years, $n=34$; age 50–59 years, $n=17$; age 60–69 years, $n=13$) and used to analyze AD protein network module changes with age. Brains were obtained from Johns Hopkins University. **b**, A synthetic eigenprotein was created for each AD network module as described in Extended Data Fig. 5 and measured by age group (left box plot) as well as correlated with age (right scatter-plot) in the aging brain cohort. Synthetic eigenprotein analyses for modules M1, M3, M4 and M10 are shown. Analyses for all modules are provided in Supplementary Fig. 9. Differences in module synthetic eigenproteins by age grouping were assessed by Kruskal–Wallis one-way ANOVA. Synthetic eigenprotein correlations were performed using biweight midcorrelation. Box plots represent the median, 25th and 75th percentiles and whiskers represent measurements to the 5th and 95th percentiles.

targeted PRM protein measurements by AD consensus module and assessed eigenprotein changes by disease category (Extended Data Fig. 6c, Supplementary Fig. 12 and Supplementary Table 4). We observed very similar AD network module changes across diseases compared to the untargeted measurements, validating the findings from the untargeted LFQ measurements. These results indicate that certain AD network modules are affected to a greater extent in AD compared to other neurodegenerative diseases and that FTLD and CBD show many similar changes to AD, with the caveat that not all neurodegenerative diseases affect the DLPFC region equally at end stages of disease.

M4 astrocyte/microglial metabolism module is enriched in AD genetic risk factors and markers of anti-inflammatory disease-associated microglia. We applied an algorithm to calculate a weighted disease risk score for proteins according to their linkage disequilibrium with AD-associated single nucleotide polymorphisms discovered through AD genome-wide association studies (GWASs)²⁵. We then calculated whether a given AD network module was enriched in these risk factor proteins. We found that the M2 myelin/oligodendrocyte and M4 astrocyte/microglial metabolism modules were significantly enriched in gene products contained within AD risk

factor loci (Fig. 5a), suggesting that the biological functions or processes reflected by these protein coexpression modules may serve causative roles in AD.

Given the strong AD trait associations of the M4 astrocyte/microglial metabolism module and its enrichment in AD genetic risk factors, we more deeply investigated the cell type nature of this coexpression module. Although expression of the M4 astrocyte/microglia metabolism module is increased with progression from a normal to an AD disease state and a majority of the most significantly increased proteins in AD are members of this module (Extended Data Fig. 7), it is unclear whether these glial responses are deleterious or protective. To better understand the role of glial cell type responses in AD, we first examined differential expression of astrocyte and microglia protein markers in AD brain by the types of cellular phenotypes with which they are associated in AD animal models^{26–31}. We found that for both astrocytic markers (Extended Data Fig. 8) and microglial markers (Extended Data Fig. 9), there appeared to be a bias toward expression of markers that are generally considered to be protective. We formally tested this observation with marker over-representation analysis in the AD network (Fig. 5b and Supplementary Table 5). Microglial protein markers that are increased in response to amyloid- β plaques but decreased

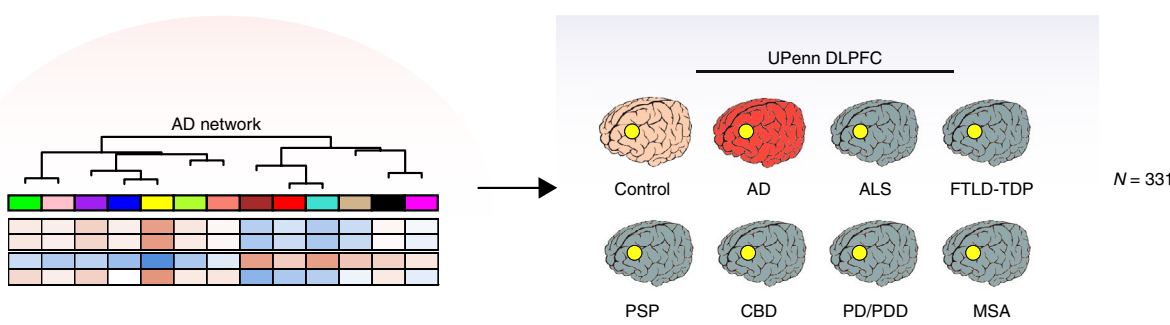
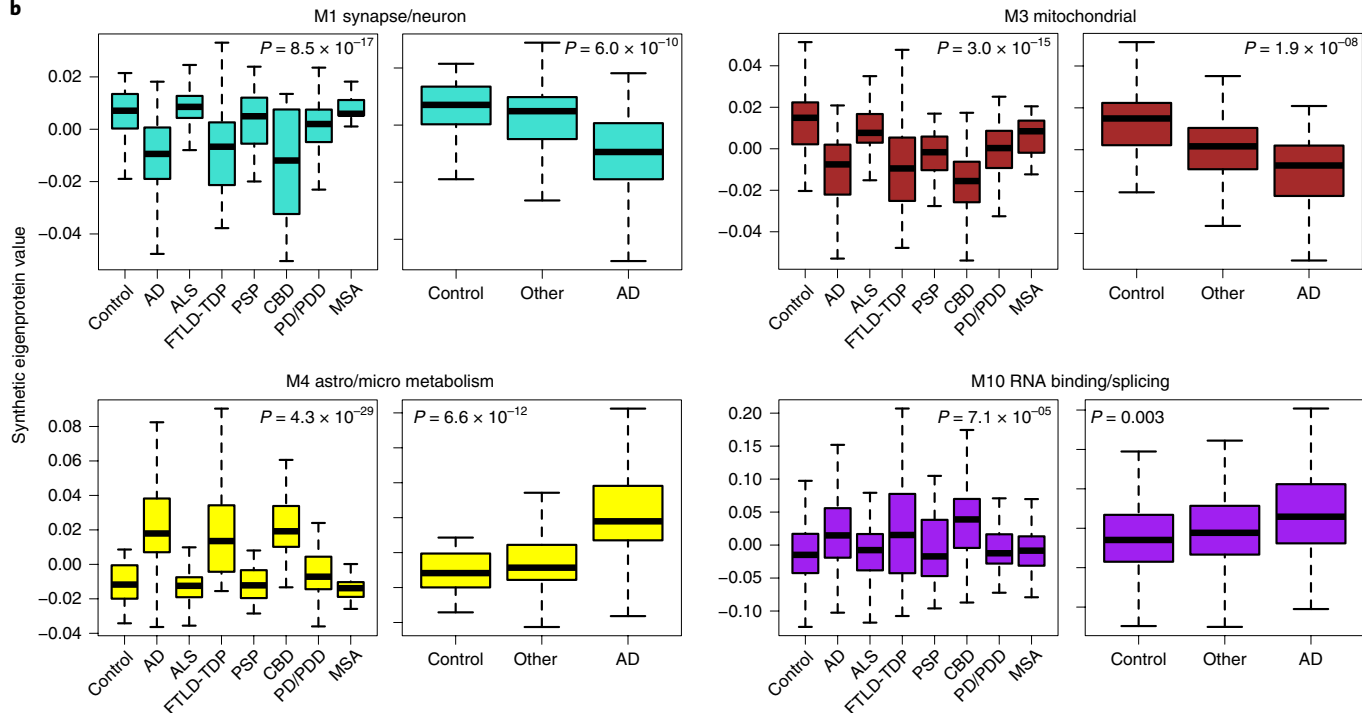
a**b**

Fig. 4 | AD protein network module changes in other neurodegenerative diseases. a, Protein levels were measured in DLPFC from controls ($n=46$) and individuals with AD ($n=49$); ALS ($n=59$); FTLD-TDP DNA-binding protein 43 inclusions ($n=29$); PSP ($n=27$); CBD ($n=17$); PD/PDD ($n=81$); and MSA ($n=23$) from the University of Pennsylvania (UPenn) Brain Bank and used to analyze AD protein network module changes in different neurodegenerative diseases. **b,** A synthetic eigenprotein was created for each AD network module as described in Extended Data Fig. 5 and measured by disease group in the UPenn cohort. Synthetic eigenprotein analyses for modules M1, M3, M4 and M10 are shown. Analyses for all modules are provided in Supplementary Fig. 10. Differences in module synthetic eigenproteins were assessed by Kruskal-Wallis one-way ANOVA. Differences between AD and other case groups were assessed by two-sided Dunnett's test, the results of which are provided in Supplementary Table 4. Box plots represent the median, 25th and 75th percentiles and whiskers represent measurements to the 5th and 95th percentiles.

in response to LPS—or markers of anti-inflammatory disease-associated microglia²⁷—were significantly enriched in the M4 module. Astrocyte markers were more mixed in module M4, with a majority of markers being shared between deleterious A1 and protective A2 phenotypes²⁶. Astrocyte and microglia phenotype markers that overlap with the top 100 proteins by module eigenprotein correlation value in the M4 module are shown in Fig. 5c. The majority of these markers were from microglia (Supplementary Table 5). To further validate these findings, we analyzed whether these markers were increased at both the transcript and protein levels in acutely isolated microglia from AD mouse models^{32,33}. The top 30 most differentially abundant microglial transcripts corresponding to proteins in the M4 module were found to be heavily biased toward an anti-inflammatory phenotype (Fig. 5d and Supplementary Table 5). Furthermore, many of the disease-associated M4 microglial protein markers were found to be increased in microglia undergoing active amyloid plaque phagocytosis (Extended Data Fig. 10 and

Supplementary Table 5)³³. In summary, we found that the M4 astrocyte/microglial metabolism module was enriched in AD genetic risk factors and that microglia cell type markers within M4 appeared to be biased towards a protective anti-inflammatory, rather than a deleterious proinflammatory, microglial phenotype.

M4 astrocyte/microglial metabolism proteins are increased in cerebrospinal fluid. To explore whether proteins from the M4 astrocyte/microglial metabolism module might also be able to serve as AD fluid biomarkers, we analyzed cerebrospinal fluid (CSF) from two separate cohorts: one cohort of 297 individuals consisting of controls and patients with AD (Cohort 1) and a second cohort of 96 individuals classified into control, AsymAD and AD (Cohort 2). Individuals in both cohorts were classified by the 'A/T/N' AD biomarker classification framework (Fig. 6a)³⁴. CSF from both cohorts was analyzed using a TMT-MS approach without previous pre-fractionation and without depletion of highly abundant proteins.

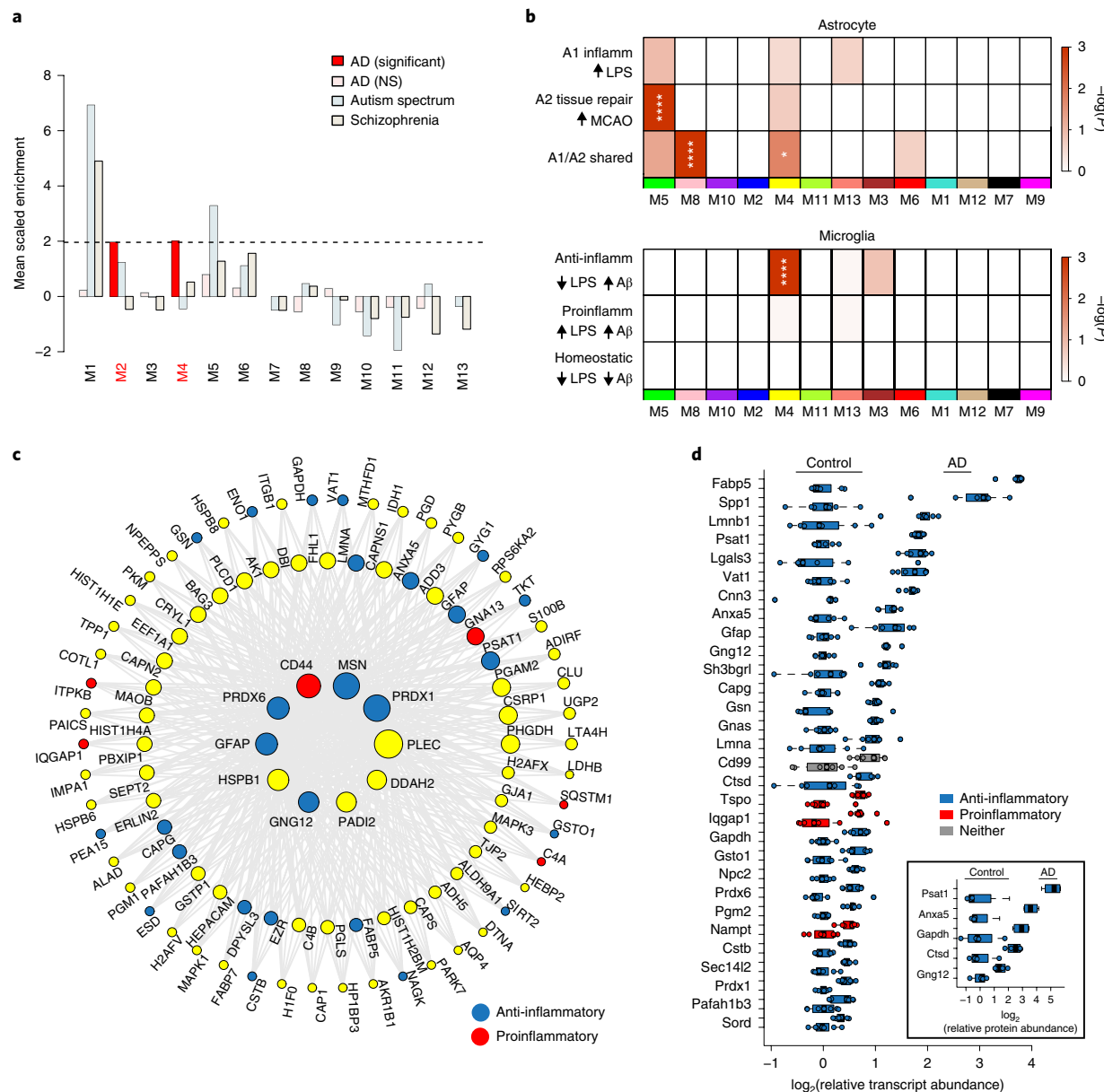


Fig. 5 | The M4 astrocyte/microglial metabolism module is enriched in AD genetic risk factors and markers of anti-inflammatory disease-associated microglia. **a**, Enrichment of proteins contained within genomic regions identified by GWAS as risk factors for AD, autism spectrum disorder and schizophrenia was calculated for each module in the AD protein network. Modules highlighted in dark red were significantly enriched for AD risk factors and not for risk factors associated with autism spectrum disorders or schizophrenia. The horizontal dotted line indicates a z score level of enrichment of 1.96 or FDR q value <0.05, above which enrichment was considered statistically significant. Enrichment was calculated using the MAGMA algorithm, as previously described¹⁷, using module proteins provided in Supplementary Table 2 and 1,234 genes identified as risk factors for AD³⁶. **b**, Enrichment of astrocyte (top) and microglia (bottom) phenotypic markers in AD protein network modules. Astrocyte phenotype markers indicating upregulation in response to acute injury with lipopolysaccharide (LPS) (A1 inflammatory), middle cerebral artery occlusion (MCAO) (A2 tissue repair) or both types of acute injury (A1/A2 shared) in a mouse model²⁶ were assessed for enrichment in AD network modules (top). Microglia markers from an mRNA coexpression analysis that are altered after challenge with LPS and/or amyloid- β plaque deposition in mouse models²⁷ were assessed for enrichment in AD network modules (anti-inflammatory, decrease with LPS administration and increase with plaque deposition; proinflammatory, increase with LPS administration and increase with plaque deposition; homeostatic, decrease with LPS administration and decrease with plaque deposition) (bottom). Module enrichment was determined by one-sided Fisher's exact test with Benjamini-Hochberg correction. Cell phenotype marker lists and protein module membership lists used for enrichment calculations are provided in Supplementary Table 5 and Supplementary Table 2, respectively. NS, not significant; *P < 0.05, **P < 0.01, ***P < 0.001, ****P < 0.0001. Exact P values are provided in Supplementary Table 5. **c**, The top 100 proteins by module eigenprotein correlation value (kME) in module M4. The size of each circle indicates the relative kME. Proteins with the largest kME are considered as 'hub' proteins within the module. Proteins highlighted in blue are upregulated in A2 tissue repair astrocyte and anti-inflammatory microglia; proteins highlighted in red are upregulated in A1 inflammatory astrocyte and proinflammatory microglia. Additional such proteins are provided in Supplementary Table 5. **d**, The top 30 most differentially abundant microglial transcripts in an AD mouse model³² that overlap with proteins in the M4 module, colored as shown in **c** ($n=7$ APP/PS1 (AD) mice, $n=7$ wild-type (ctrl) mice). M4 proteins that overlap with transcripts elevated in microglia undergoing active amyloid- β plaque phagocytosis³³ are provided in Extended Data Fig. 10. Transcript elevations validated at the protein level in microglia undergoing active amyloid- β plaque phagocytosis³³ ($n=4$ 5xFAD (AD) mice, $n=4$ wild-type (ctrl) mice) (inset). Box plots represent the median, 25th and 75th percentiles and whiskers represent measurements to the 5th and 95th percentiles.

In Cohort 1, we observed 22 proteins that mapped to the M4 astrocyte/microglial metabolism module in the brain (Supplementary Fig. 13). All of them showed either an increase in AD or no change, with ten reaching statistical significance at $P < 0.05$. The most significantly increased M4 module proteins observed in Cohort 1 are shown in Fig. 6b and include the M4 hub proteins CD44, peroxiredoxin-1 (PRDX1) and dimethylarginine dimethylaminohydrolase-2 (DDAH2), in addition to the metabolic proteins, lactate dehydrogenase B-chain (LDHB) and pyruvate kinase (PKM) involved in glycolysis. To validate these findings and to assess whether the observed changes in CSF levels of M4 proteins occur before development of cognitive impairment, we analyzed individuals in Cohort 2, approximately one-third of whom had AsymAD. AsymAD was defined as CSF levels of amyloid- β , total tau and phospho-tau consistent with an AD diagnosis, but without cognitive impairment. In Cohort 2, 27 proteins mapped to the M4 astrocyte/microglial metabolism module in the brain (Supplementary Fig. 14). Of these 27, 17 overlapped with M4 proteins measured in discovery Cohort 1 and showed the same direction of change in AD CSF. In addition, many also showed significant or trend elevations in AsymAD, including CD44, LDHB and PKM and correlated with cognitive function (Fig. 6c). In summary, multiple M4 astrocyte/microglial metabolism module protein members could be measured in human CSF by MS without fractionation or previous depletion of highly abundant proteins. A number of these proteins were elevated in AsymAD and AD, including M4 hub proteins CD44, PRDX1 and DDAH2.

Discussion

In this study, we analyzed more than 2,000 brains by MS-based proteomics to arrive at a consensus view of the proteomic changes that occur in brain during progression from normal to asymptomatic and symptomatic AD states. We find that the protein coexpression families most strongly correlated to disease reflect synaptic, mitochondrial, RNA binding/splicing and astrocyte/microglial metabolism biological functions, with astrocyte/microglial metabolism most significantly associated with AD compared to other biological processes and functions. Increases in expression level of the M4 astrocyte/microglial metabolism module are observed with aging, but are stronger in AD, reflecting shared biology between ‘normal’ aging and AD. The M4 module is enriched in AD genetic risk factors, indicating a potential causative role for this protein coexpression module in disease pathogenesis and appears to serve a protective anti-inflammatory function in model systems, suggesting that genetic risk factor polymorphisms that cluster in this module may induce a loss-of-function phenotype. M4 astrocyte/microglial module proteins are increased in AsymAD and AD CSF, suggesting that proteins within the M4 module may serve as useful biomarkers for staging AD progression and for development of novel therapeutic approaches to the disease.

The protein coexpression modules we identified are not significantly influenced by regional tissue variation among temporal

cortex, precuneus and DLPFC brain regions. Indeed, we observed that all of the larger modules were highly preserved in both temporal cortex and precuneus, with preservation P values approaching zero in both regions. This suggests that the biological processes and cell types driving the coexpression patterns in AD brain are highly shared among these brain regions. Future proteomic analyses that include other brain regions less affected in late-onset AD (for example, visual cortex) would be informative to further explore potential protective processes that may be important for regional vulnerability in AD. Also, emerging analyses that employ the use of newer MS-based proteomic approaches, such as TMT-MS, that allow for pre-fractionation of brain tissue peptides before analysis to increase the depth of proteome coverage will likely lead to identification of additional disease-related coexpression modules^{35–38}. A recent proteomic study by Bai et al. on a smaller number of AD brains employed TMT-MS to deeply profile the AD brain proteome and used network analysis to identify biological pathways altered in AD³⁵. Cell type regression was performed before network analysis by Bai et al. from pooled samples and therefore, the protein network described here is not directly comparable to the one described by Bai et al. However, for proteins in this study that overlap with the validated set of differentially expressed proteins described by Bai et al. obtained after cell type regression, a majority are also differentially expressed in AD and map to the M4 module.

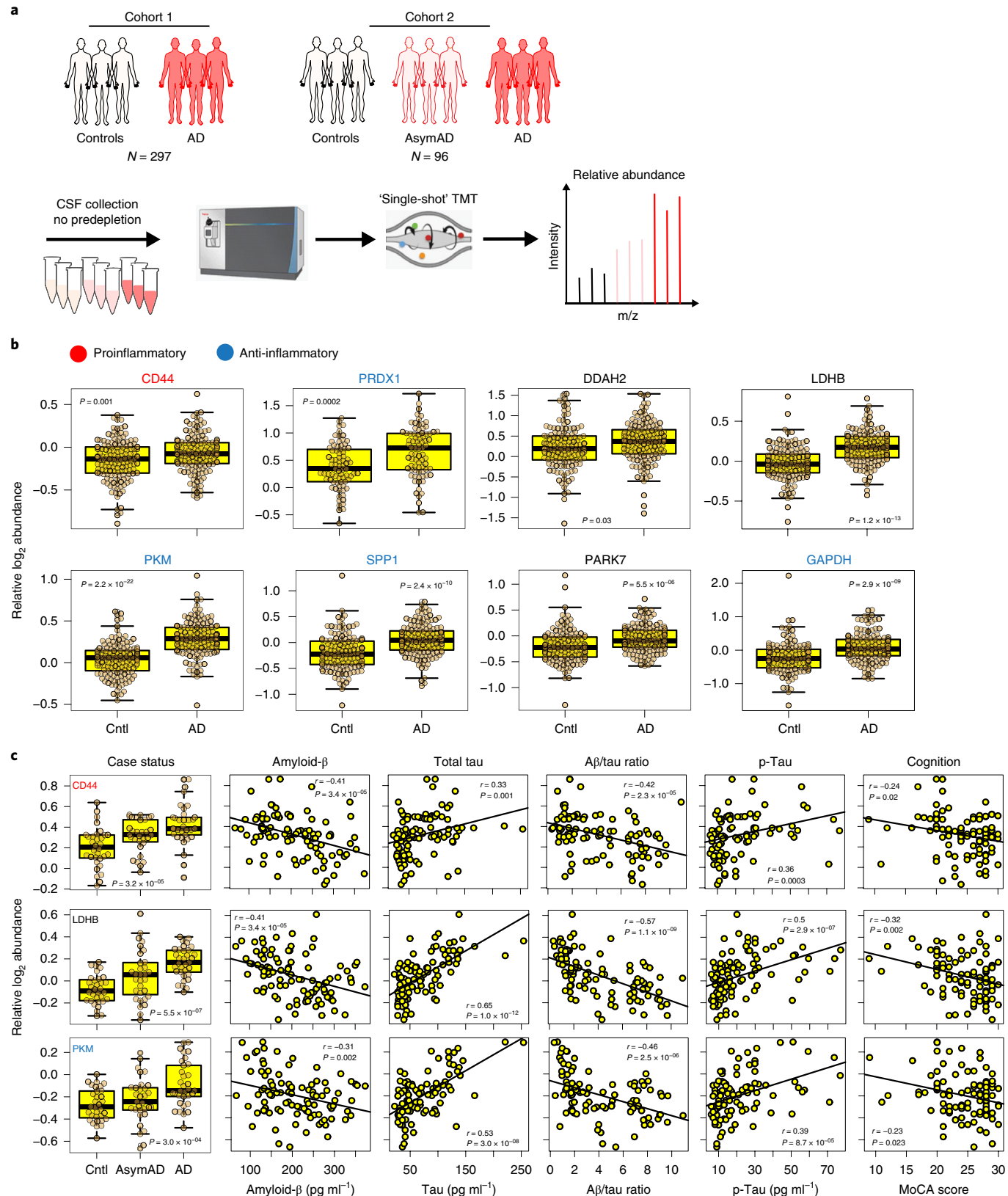
We assessed disease specificity of the AD protein coexpression network by analyzing how the protein network modules changed in six other neurodegenerative diseases, encompassing diverse brain pathologies. One caveat to this analysis is that we analyzed only DLPFC, which is not equally affected in all the neurodegenerative diseases we assessed. With this caveat in mind, we observed that FTLD-TDP and CBD had the most similar network changes to AD, suggesting that these clinicopathologic entities are fundamentally related to AD at the brain proteomic level. A proteomic relationship between AD and frontotemporal dementia (FTD) is supported by the fact that mutations in the triggering receptor expressed on myeloid cells 2 protein cause microglial dysfunction and lead to AD^{39,40}, whereas mutations in the progranulin protein also cause microglial dysfunction and lead to FTD^{41–43}. Further studies comparing frontal predominant AD, FTLD-TDP and FTLD-tau cases would be informative to assess the degree to which the underlying neuropathology observed at autopsy is related to differences in proteomic network changes in the DLPFC region.

A key finding from our proteomic study is that glial biology—and microglial biology in particular—is a likely causal driver of AD pathogenesis. This finding is consistent with the results of other recent protein coexpression analyses of AD^{17,44}. The AD protein network module most strongly associated with AD is enriched in astrocyte and microglial proteins and is also enriched in proteins associated with genetic risk for AD. The M4 astrocyte/microglial metabolism module increases in AsymAD and correlates most strongly with cognitive impairment, suggesting that the biological

Fig. 6 | M4 astrocyte/microglial metabolism module protein levels are elevated in AsymAD and AD CSF. **a**, Approach to analysis of M4 proteins in CSF from two different cohorts. CSF in Cohort 1 ($n = 297$ biologically independent samples) was obtained from individuals with normal CSF amyloid- β and tau levels (controls, $n = 150$ samples) and patients with low amyloid- β , elevated tau levels and cognitive impairment (AD, $n = 147$ samples). CSF in cohort 2 ($n = 96$ biologically independent samples) was obtained from controls ($n = 32$ samples) and patients with AD ($n = 33$ samples) as defined in Cohort 1, as well as individuals with CSF amyloid- β and tau levels that met criteria for AD but who were cognitively healthy at the time of collection (AsymAD, $n = 31$ samples). CSF was analyzed without previous pre-fractionation or depletion of highly abundant proteins; relative protein levels were measured by TMT-MS. **b**, Relative CSF protein levels of selected M4 module members in cohort 1. Protein names are colored according to proinflammatory (red) or anti-inflammatory (blue) classification. Proteins that are considered neither pro- nor anti-inflammatory are in black. Additional M4 protein measurements, as well as trait correlations for the measured proteins, are provided in Supplementary Fig. 13. **c**, Relative CSF protein levels of selected M4 module members in cohort 2. Protein names are colored as in **b**. Additional measurements and trait correlations are provided in Supplementary Fig. 14. Differences in protein levels were assessed by two-sided Welch's t -test (**b**) or Kruskal-Wallis one-way ANOVA (**c**). Correlations were performed using biweight midcorrelation. Box plots represent the median, 25th and 75th percentiles and whiskers represent measurements to the 5th and 95th percentiles. MoCA, Montreal Cognitive Assessment (higher scores represent better cognitive function).

changes reflected by this module occur early in the disease and have significant functional consequence on progression to dementia. A natural assumption would be that increases in M4 module expression levels are deleterious to brain health and that potential therapies targeting reduction of M4 would likely be beneficial in AD.

However, several lines of evidence support a possible protective role of this coexpression module. An important observation is that AD genetic risk alleles, which are more likely to cause loss-of-function changes rather than gain-of-function changes, are enriched in the M4 module. The M4 module is also enriched in microglial markers



that are upregulated in response to amyloid- β deposition and downregulated in response to LPS, indicating that the microglial response as reflected in M4 module expression is likely biased towards an anti-inflammatory disease-associated phenotype²⁷. Many M4 proteins are elevated in microglia that are undergoing plaque phagocytosis, which is consistent with the strong association of M4 expression with Consortium to Establish a Registry for Alzheimer's disease (CERAD) score. Notably, when we compare our findings to a previous proteomic study that quantified levels of plaque-associated proteins in normal versus rapidly-progressive AD⁴⁵, seven out of the top ten plaque-associated proteins most significantly decreased in rapidly progressive AD are found in the M4 module, including M4 hubs MSN and PLEC. This is consistent with the finding that early microglial activation in response to amyloid plaques, as assessed by in vivo microglial imaging studies, is correlated with increased gray matter volume and reduced rate of cognitive decline^{46,47}. Notably, the degree of astrogliosis surrounding plaques seems to be positively correlated with improved cognitive function not only in AD, but also in normal aging individuals⁴⁸. Taken together, these findings suggest that lack of an M4 astrocyte/microglial response to plaques in preclinical or clinical AD may lead to more rapid cognitive decline.

Many of the most significantly elevated M4 proteins in CSF are involved in glycolysis, including LDHB, PKM and glyceraldehyde 3-phosphate dehydrogenase. Elevations in PRDX1, DDAH and protein/nucleic acid deglycase DJ-1 were also observed, all of which are important antioxidant effector proteins^{49–51} and are likely to be elevated in concert with increased glycolytic flux. LDHB, PKM and DDAH1 have recently been reported as promising AD CSF biomarkers^{52,53}. While M4 markers may not be entirely specific for AD, given elevation of the M4 module in FTD and CBD, they may allow for assessment of an injury response in AD in conjunction with amyloid and tau biomarkers and serve as useful biomarkers for other neurodegenerative dementias in addition to AD. Measurement of additional M4 markers in biofluids is undoubtedly possible, as our MS measurements were performed on unfractionated CSF not depleted of highly abundant proteins. Indeed, recent studies have identified a number of additional potential biomarkers from M4 and other brain modules by deep MS-based discovery on fractionated CSF^{35,36,54}. Monitoring multiple M4 protein levels in biofluid may provide a robust measure of target engagement for AD therapies.

In summary, our comprehensive study on more than 2,000 brains and nearly 400 CSF samples provides a consensus view of the proteomic network landscape of AD and the biological changes associated with asymptomatic and symptomatic stages of the disease and highlights the central role of glial biology in pathogenesis of the disease. Programs that target this biology hold promise for AD drug therapy and biomarker development, especially those that target pro- and anti-inflammatory astrocytes and microglia.

Online content

Any methods, additional references, Nature Research reporting summaries, source data, extended data, supplementary information, acknowledgements, peer review information; details of author contributions and competing interests; and statements of data and code availability are available at <https://doi.org/10.1038/s41591-020-0815-6>.

Received: 11 October 2019; Accepted: 27 February 2020;

Published online: 13 April 2020

References

1. Prince, M. et al. *World Alzheimer Report 2015: The Global Impact of Dementia*. (Alzheimer's Disease International, 2015).
2. Jack, C. R. Jr. et al. NIA-AA research framework: toward a biological definition of Alzheimer's disease. *Alzheimers Dement.* **14**, 535–562 (2018).
3. Miller, J. A., Oldham, M. C. & Geschwind, D. H. A systems level analysis of transcriptional changes in Alzheimer's disease and normal aging. *J. Neurosci.* **28**, 1410–1420 (2008).
4. Oldham, M. C. et al. Functional organization of the transcriptome in human brain. *Nat. Neurosci.* **11**, 1271–1282 (2008).
5. Clarke, C. et al. Correlating transcriptional networks to breast cancer survival: a large-scale coexpression analysis. *Carcinogenesis* **34**, 2300–2308 (2013).
6. Barabasi, A. L., Gulbahce, N. & Loscalzo, J. Network medicine: a network-based approach to human disease. *Nat. Rev. Genet.* **12**, 56–68 (2011).
7. Huan, T. et al. Integrative network analysis reveals molecular mechanisms of blood pressure regulation. *Mol. Syst. Biol.* **11**, 799 (2015).
8. Tran, L. M. et al. Inferring causal genomic alterations in breast cancer using gene expression data. *BMC Syst. Biol.* **5**, 121 (2011).
9. Huan, T. et al. A systems biology framework identifies molecular underpinnings of coronary heart disease. *Arterioscler. Thromb. Vasc. Biol.* **33**, 1427–1434 (2013).
10. Cerami, E., Demir, E., Schultz, N., Taylor, B. S. & Sander, C. Automated network analysis identifies core pathways in glioblastoma. *PLoS ONE* **5**, e8918 (2010).
11. Yue, Z. et al. Repositioning drugs by targeting network modules: a Parkinson's disease case study. *BMC Bioinformatics* **18**, 532 (2017).
12. Toledo, J. B. et al. Metabolic network failures in Alzheimer's disease: a biochemical road map. *Alzheimers Dement.* **13**, 965–984 (2017).
13. Sun, M., Sun, T., He, Z. & Xiong, B. Identification of two novel biomarkers of rectal carcinoma progression and prognosis via co-expression network analysis. *Oncotarget* **8**, 69594–69609 (2017).
14. He, Z. et al. Identifying biomarkers of papillary renal cell carcinoma associated with pathological stage by weighted gene co-expression network analysis. *Oncotarget* **8**, 27904–27914 (2017).
15. Mirra, S. S. et al. The Consortium to Establish a Registry for Alzheimer's Disease (CERAD). Part II. Standardization of the neuropathologic assessment of Alzheimer's disease. *Neurology* **41**, 479–486 (1991).
16. Miller, J. A., Woltjer, R. L., Goodenbour, J. M., Horvath, S. & Geschwind, D. H. Genes and pathways underlying regional and cell type changes in Alzheimer's disease. *Genome Med.* **5**, 48 (2013).
17. Seyfried, N. T. et al. A multi-network approach identifies protein-specific co-expression in asymptomatic and symptomatic Alzheimer's disease. *Cell Syst.* **4**, 60–72.e64 (2017).
18. Bennett, D. A., Schneider, J. A., Arvanitakis, Z. & Wilson, R. S. Overview and findings from the religious orders study. *Curr. Alzheimer Res.* **9**, 628–645 (2012).
19. Bennett, D. A. et al. Overview and findings from the rush memory and aging project. *Curr. Alzheimer Res.* **9**, 646–663 (2012).
20. Bennett, D. A. et al. The Rush Memory and Aging Project: study design and baseline characteristics of the study cohort. *Neuroepidemiology* **25**, 163–175 (2005).
21. Ping, L. et al. Global quantitative analysis of the human brain proteome in Alzheimer's and Parkinson's Disease. *Sci. Data* **5**, 180036 (2018).
22. Rauniyar, N. & Yates, J. R. 3rd Isobaric labeling-based relative quantification in shotgun proteomics. *J. Proteome Res.* **13**, 5293–5309 (2014).
23. Ting, L., Rad, R., Gygi, S. P. & Haas, W. MS3 eliminates ratio distortion in isobaric multiplexed quantitative proteomics. *Nat. Methods* **8**, 937–940 (2011).
24. Peterson, A. C., Russell, J. D., Bailey, D. J., Westphall, M. S. & Coon, J. J. Parallel reaction monitoring for high resolution and high mass accuracy quantitative, targeted proteomics. *Mol. Cell Proteomics* **11**, 1475–1488 (2012).
25. de Leeuw, C. A., Mooij, J. M., Heskes, T. & Posthuma, D. MAGMA: generalized gene-set analysis of GWAS data. *PLoS Comput. Biol.* **11**, e1004219 (2015).
26. Zamani, J. L. et al. Genomic analysis of reactive astrogliosis. *J. Neurosci.* **32**, 6391–6410 (2012).
27. Rangaraju, S. et al. Identification and therapeutic modulation of a pro-inflammatory subset of disease-associated-microglia in Alzheimer's disease. *Mol. Neurodegener.* **13**, 24 (2018).
28. Ransohoff, R. M. & Perry, V. H. Microglial physiology: unique stimuli, specialized responses. *Annu. Rev. Immunol.* **27**, 119–145 (2009).
29. Butovsky, O. et al. Identification of a unique TGF- β -dependent molecular and functional signature in microglia. *Nat. Neurosci.* **17**, 131–143 (2014).
30. Holtzman, D. M. et al. Induction of a common microglia gene expression signature by aging and neurodegenerative conditions: a co-expression meta-analysis. *Acta Neuropathol. Commun.* **3**, 31 (2015).
31. Hammond, T. R. et al. Single-cell RNA sequencing of microglia throughout the mouse lifespan and in the injured brain reveals complex cell-state changes. *Immunity* **50**, 253–271 (2019).
32. Orre, M. et al. Isolation of glia from Alzheimer's mice reveals inflammation and dysfunction. *Neurobiol. Aging* **35**, 2746–2760 (2014).
33. Grubman, A. et al. Mouse and human microglial phenotypes in Alzheimer's disease are controlled by amyloid plaque phagocytosis through Hif1 α . Preprint at *bioRxiv* <https://doi.org/10.1101/639054>
34. Jack, C. R. Jr. et al. A/T/N: an unbiased descriptive classification scheme for Alzheimer disease biomarkers. *Neurology* **87**, 539–547 (2016).
35. Bai, B. et al. Deep multilayer brain proteomics identifies molecular networks in Alzheimer's disease progression. *Neuron* **105**, 975–991.e7 (2020).

36. Higginbotham, L., et al. Integrated proteomics reveals brain-based cerebrospinal fluid biomarkers in asymptomatic and symptomatic Alzheimer's disease. Preprint at *bioRxiv* <https://doi.org/10.1101/806752>
37. Johnson, E. C. B., et al. Deep proteomic network analysis of Alzheimer's disease brain reveals alterations in RNA binding proteins and RNA splicing associated with disease. *Mol. Neurodegener.* **13**, 52 (2018).
38. Wingo, A. P., et al. Cerebral atherosclerosis contributes to Alzheimer's dementia independently of its hallmark amyloid and tau pathologies. Preprint at *bioRxiv* <https://doi.org/10.1101/793349>
39. Jonsson, T., et al. Variant of TREM2 associated with the risk of Alzheimer's disease. *N. Engl. J. Med.* **368**, 107–116 (2013).
40. Wang, Y., et al. TREM2 lipid sensing sustains the microglial response in an Alzheimer's disease model. *Cell* **160**, 1061–1071 (2015).
41. Baker, M., et al. Mutations in progranulin cause tau-negative frontotemporal dementia linked to chromosome 17. *Nature* **442**, 916–919 (2006).
42. Cruts, M., et al. Null mutations in progranulin cause ubiquitin-positive frontotemporal dementia linked to chromosome 17q21. *Nature* **442**, 920–924 (2006).
43. Hickman, S., Izzy, S., Sen, P., Morsett, L. & El Khoury, J. Microglia in neurodegeneration. *Nat. Neurosci.* **21**, 1359–1369 (2018).
44. Swarup, V., et al. Identification of conserved proteomic networks in neurodegenerative dementia. Preprint at *bioRxiv* <https://doi.org/10.1101/825802>
45. Drummond, E., et al. Proteomic differences in amyloid plaques in rapidly progressive and sporadic Alzheimer's disease. *Acta Neuropathol.* **133**, 933–954 (2017).
46. Hamelin, L., et al. Early and protective microglial activation in Alzheimer's disease: a prospective study using ¹⁸F-DPA-714 PET imaging. *Brain* **139**, 1252–1264 (2016).
47. Ramanan, V. K., et al. GWAS of longitudinal amyloid accumulation on ¹⁸F-florbetapir PET in Alzheimer's disease implicates microglial activation gene IL1RAP. *Brain* **138**, 3076–3088 (2015).
48. Mathur, R., et al. A reduced astrocyte response to β -amyloid plaques in the ageing brain associates with cognitive impairment. *PLoS ONE* **10**, e0118463 (2015).
49. Luo, Y., et al. Asymmetric dimethylarginine exacerbates $\alpha\beta$ -induced toxicity and oxidative stress in human cell and *Caenorhabditis elegans* models of Alzheimer disease. *Free Radic. Biol. Med.* **79**, 117–126 (2015).
50. Power, J. H., et al. Peroxiredoxin 6 in human brain: molecular forms, cellular distribution and association with Alzheimer's disease pathology. *Acta Neuropathol.* **115**, 611–622 (2008).
51. Clements, C. M., McNally, R. S., Conti, B. J., Mak, T. W. & Ting, J. P. DJ-1, a cancer- and Parkinson's disease-associated protein, stabilizes the antioxidant transcriptional master regulator Nrf2. *Proc. Natl Acad. Sci. USA* **103**, 15091–15096 (2006).
52. Dayon, L., et al. Alzheimer disease pathology and the cerebrospinal fluid proteome. *Alzheimers Res. Ther.* **10**, 66 (2018).
53. Sathe, G., et al. Quantitative proteomic profiling of cerebrospinal fluid to identify candidate biomarkers for Alzheimer's disease. *Proteomics Clin. Appl.* **13**, e1800105 (2019).
54. Dayon, L., et al. Proteomes of paired human cerebrospinal fluid and plasma: relation to blood-brain barrier permeability in older adults. *J. Proteome Res.* **18**, 1162–1174 (2019).
55. Langfelder, P., Luo, R., Oldham, M. C. & Horvath, S. Is my network module preserved and reproducible? *PLoS Comput. Biol.* **7**, e1001057 (2011).
56. Lambert, J. C., et al. Meta-analysis of 74,046 individuals identifies 11 new susceptibility loci for Alzheimer's disease. *Nat. Genet.* **45**, 1452–1458 (2013).

Publisher's note Springer Nature remains neutral with regard to jurisdictional claims in published maps and institutional affiliations.

This is a U.S. government work and not under copyright protection in the U.S.; foreign copyright protection may apply 2020

Methods

Brain tissue samples and case classification. Brain tissue used in this study was obtained from the autopsy collections of the BLSA⁵⁷, Banner⁵⁸, MSSB, ACT, Mayo Clinic Brain Bank, ROS/MAP⁵⁹, University of Pennsylvania School of Medicine Brain Bank and the Baltimore Coroner's Office. Tissue was from the dorsolateral prefrontal cortex (Brodmann Area 9 where available) or temporal cortex and precuneus regions where indicated. Human postmortem tissues were acquired under Institutional Review Board protocols at each respective institution. Postmortem neuropathological evaluation of neuritic plaque distribution was performed according to CERAD criteria¹⁵, while extent of spread of neurofibrillary tangle pathology was assessed with the Braak staging system⁶⁰. Other neuropathologic diagnoses were made in accordance with established criteria and guidelines⁶¹. All case metadata, including age, sex, PMI, cognitive function, APOE genotype, neuropathological criteria and disease status, are provided in Supplementary Table 1. Case classification harmonization across cohorts was performed using the following rubric: cases with CERAD 0–1 and Braak 0–3 without dementia at last evaluation were defined as control (if Braak equals 3, then CERAD must equal 0); cases with CERAD 1–3 and Braak 3–6 without dementia at last evaluation were defined as AsymAD; cases with CERAD 2–3 and Braak 3–6 with dementia at last evaluation were defined as AD. Dementia was defined as MMSE < 24, Cognitive Abilities Screening Instrument (CASI) score < 81 or CDR ≥ 1, based on previous comparative study⁶². Mayo and University of Pennsylvania cases were not included in the case harmonization scheme, and therefore preservation of consensus network modules in these cohorts provides an additional degree of robustness.

Brain tissue homogenization and protein digestion. Procedures for tissue homogenization for all tissues were performed essentially as described^{17,21}. Approximately 100 mg (wet tissue weight) of brain tissue was homogenized in 8 M urea lysis buffer (8 M urea, 10 mM Tris, 100 mM NaHPO₄, pH 8.5) with HALT protease and phosphatase inhibitor cocktail (Thermo Fisher Scientific) using a Bullet Blender (NextAdvance). Each Rino sample tube (NextAdvance) was supplemented with ~100 µl of stainless steel beads (0.9 to 2.0 mm blend, NextAdvance) and 500 µl of lysis buffer. Tissues were added immediately after excision and samples were then placed into the bullet blender at 4°C. The samples were homogenized for two full 5-min cycles and the lysates were transferred to new Eppendorf Lobind tubes. Each sample was then sonicated for three cycles consisting of 5 s of active sonication at 30% amplitude, followed by 15 s on ice. Samples were then centrifuged for 5 min at 15,000g and the supernatant was transferred to a new tube. Protein concentration was determined by bicinchoninic acid assay (Pierce). For protein digestion, 100 µg of each sample was aliquoted and volumes were normalized with additional lysis buffer. For the ROS/MAP cohort, an equal amount of protein from each sample was aliquoted and digested in parallel to serve as the global pooled internal standard (GIS) in each TMT batch, as described below. Similarly, GIS pooled standards were generated from the Banner, MSSB, Mayo, Aging and UPenn cohorts. Samples were reduced with 1 mM dithiothreitol at room temperature for 30 min, followed by 5 mM iodoacetamide alkylation in the dark for another 30 min. Lysyl endopeptidase (Wako) at 1:100 dilution (w/w) was added and digestion was allowed to proceed overnight. Samples were then diluted sevenfold with 50 mM ammonium bicarbonate. Trypsin (Promega) was added at 1:50 dilution (w/w) and digestion was carried out for another 16 h. The peptide solutions were acidified to a final concentration of 1% (vol/vol) formic acid (FA) and 0.1% (vol/vol) trifluoroacetic acid (TFA), and desalted with a 30-mg HLB column (Oasis). Each HLB column was first rinsed with 1 ml of methanol, washed with 1 ml 50% (vol/vol) acetonitrile (ACN) and equilibrated with 2 × 1 ml 0.1% (vol/vol) TFA. The samples were loaded onto the column and washed with 2 × 1 ml 0.1% (vol/vol) TFA. Elution was performed with two volumes of 0.5 ml of 50% (vol/vol) ACN.

MS analysis for label-free proteomics. MS analyses of MSSB, ACT, BLSA, Banner, Mayo and UPenn cohorts were performed on a Q-Exactive Plus mass spectrometer, essentially as described¹⁷. Brain-derived tryptic peptides (2 µg) were resuspended in peptide loading buffer (0.1% FA, 0.03% TFA, 1% ACN) containing 0.2 pmol of isotopically labeled peptide calibrants (Thermo Fisher Scientific, 88321). Peptide mixtures were separated on a self-packed C18 (1.9 µm, Dr Maisch) fused silica column (25 cm × 75 µm internal diameter; New Objective) by a NanoAcuity UHPLC (Waters) and monitored on a Q-Exactive Plus mass spectrometer (Thermo Fisher Scientific). Elution was performed over a 120-min gradient at a rate of 400 nl min⁻¹ with buffer B ranging from 3% to 80% (buffer A, 0.1% FA and 5% DMSO in water; buffer B, 0.1% FA and 5% DMSO in ACN). The MS cycle was programmed to collect one full MS scan followed by ten data-dependent MS/MS scans. The MS scans (300–1800 m/z range, 1,000,000 automatic gain control (AGC), 150 ms maximum ion time) were collected at a resolution of 70,000 at m/z 200 in profile mode and the MS/MS spectra (2 m/z isolation width, 25% collision energy, 100,000 AGC target, 50 ms maximum ion time) were acquired at a resolution of 17,500 at m/z 200. Dynamic exclusion was set to exclude previous sequenced precursor ions for 30 s within a 10-ppm window. Precursor ions with +1 and +6 or higher charge states were excluded from sequencing.

Label-free quantification. For the consensus LFQ search, 645 RAW files, including individual cases and pooled GIS samples from the MSSB, ACT, Banner

and BLSA cohorts, were uploaded onto the Amazon Web Services Cloud and analyzed using MaxQuant v.1.6.3.4 with Thermo Foundation 2.0 for RAW file reading capability. The Mayo, BLSA precuneus, Aging and UPenn cohorts were each searched separately using MaxQuant. The search engine Andromeda was used to build and search a concatenated target-decoy UniProt Knowledgebase (UniProtKB) containing both Swiss-Prot and TrEMBL human reference protein sequences (90,411 target sequences downloaded 21 April 2015), plus 245 contaminant proteins included as a parameter for the Andromeda search within MaxQuant. Methionine oxidation (+15.9949 Da), asparagine and glutamine deamidation (+0.9840 Da) and protein N-terminal acetylation (+42.0106 Da) were variable modifications (up to five allowed per peptide); cysteine was assigned a fixed carbamidomethyl modification (+57.0215 Da). Only fully tryptic peptides with up to two miscleavages were considered in the database search. A precursor mass tolerance of ±20 ppm was applied before mass accuracy calibration and ±4.5 ppm after internal MaxQuant calibration. Other search settings included a maximum peptide mass of 6,000 Da, a minimum peptide length of six residues and 0.05-Da tolerance for high resolution MS/MS scans. The FDR for peptide spectral matches, proteins and site decoy fraction was set to 1%. Quantification settings were as follows: requantify with a second peak-finding attempt after protein identification is complete; match full MS1 peaks between runs; use a 0.7-min retention time match window after an alignment function was found with a 20-min retention time search space. The LFQ algorithm in MaxQuant^{43,64} was used for protein quantitation. The quantitation method considered only razor and unique peptides for protein level quantitation. The total summed protein intensity was also used to assess overall signal drift across samples before LFQ normalization.

Isobaric TMT peptide labeling of ROS/MAP brain tissues. Before TMT labeling, individuals were randomized by covariates (such as age, sex, PMI and diagnosis), into 50 total batches (eight individuals per batch). Peptides from each individual ($n = 400$) and the GIS pooled standard ($n = 100$) were labeled using the TMT 10-plex kit (Thermo Fisher Scientific, 90406). In each batch, TMT channels 126 and 131 were used to label GIS standards, while the eight middle TMT channels were reserved for individual samples following randomization. Labeling was performed as previously described^{17,57}. Briefly, each sample (containing 100 µg of peptides) was resuspended in 100 mM triethylammonium bicarbonate (TEAB) buffer (100 µl). The TMT labeling reagents were equilibrated to room temperature and anhydrous ACN (256 µl) was added to each reagent channel. Each channel was gently vortexed for 5 min and 41 µl from each TMT channel was transferred to the peptide solutions and allowed to incubate for 1 h at room temperature. The reaction was quenched with 5% (vol/vol) hydroxylamine (8 µl) (Pierce). All ten channels were combined and dried by SpeedVac (LabConco) to approximately 150 µl and diluted with 1 ml of 0.1% (vol/vol) TFA, then acidified to a final concentration of 1% (vol/vol) FA and 0.1% (vol/vol) TFA. Peptides were desalted with a 200-mg C18 Sep-Pak column (Waters). Each Sep-Pak column was activated with 3 ml of methanol, washed with 3 ml of 50% (vol/vol) ACN and equilibrated with 2 × 3 ml of 0.1% TFA. The samples were loaded and each column was washed with 2 × 3 ml 0.1% (vol/vol) TFA, followed by 2 ml of 1% (vol/vol) FA. Elution was performed with two volumes of 1.5 ml of 50% (vol/vol) ACN. The eluates were then dried to completeness using a SpeedVac.

High-pH off-line fractionation of ROS/MAP brain tissues. High pH fractionation was performed essentially as described⁶⁵ with slight modification. Dried samples were resuspended in high-pH loading buffer (0.07% vol/vol NH₄OH, 0.045% vol/vol FA, 2% vol/vol ACN) and loaded onto an Agilent ZORBAX 300 Extend-C18 column (2.1 mm × 150 mm with 3.5 µm beads). An Agilent 1100 HPLC system was used to carry out fractionation. Solvent A consisted of 0.0175% (vol/vol) NH₄OH, 0.01125% (vol/vol) FA and 2% (vol/vol) ACN; solvent B consisted of 0.0175% (vol/vol) NH₄OH, 0.01125% (vol/vol) FA and 90% (vol/vol) ACN. The sample elution was performed over a 58.6-min gradient with a flow rate of 0.4 ml min⁻¹. The gradient consisted of 100% solvent A for 2 min, then 0% to 12% solvent B over 6 min, then 12% to 40% over 28 min, then 40% to 44% over 4 min, then 44% to 60% over 5 min and then held constant at 60% solvent B for 13.6 min. A total of 96 individual equal volume fractions were collected across the gradient and subsequently pooled by concatenation⁶⁵ into 24 fractions and dried to completeness using a SpeedVac.

TMT-MS of ROS/MAP brain tissues. All fractions were resuspended in an equal volume of loading buffer (0.1% FA, 0.03% TFA, 1% ACN) and analyzed by liquid chromatography coupled to tandem MS essentially as described⁶⁶, with slight modifications. Peptide eluents were separated on a self-packed C18 (1.9 µm, provided by Dr Maisch) fused silica column (25 cm × 75 µm internal diameter; New Objective) by an Dionex UltiMate 3000 RSLC nano liquid chromatography system (Thermo Fisher Scientific) and monitored on an Orbitrap Fusion mass spectrometer (Thermo Fisher Scientific). Sample elution was performed over a 180-min gradient with flow rate at 225 nl min⁻¹. The gradient was from 3% to 7% buffer B over 5 min, then 7% to 30% over 140 min, then 30% to 60% over 5 min, then 60% to 99% over 2 min, then held constantly at 99% solvent B for 8 min and then back to 1% B for an additional 20 min to equilibrate the column. Buffer A was water with 0.1% (vol/vol) FA and buffer B was 80% (vol/vol) acetonitrile in

water with 0.1% (vol/vol) FA. The mass spectrometer was set to acquire in data-dependent mode using the top speed workflow with a cycle time of 3 s. Each cycle consisted of one full scan followed by as many MS/MS (MS2) scans that could fit within the time window. The full scan (MS1) was performed with an m/z range of 350–1,500 at 120,000 resolution (at 200 m/z) with AGC set at 4×10^5 and maximum injection time of 50 ms. The most intense ions were selected for higher energy collision-induced dissociation at 38% collision energy with an isolation of 0.7 m/z, a resolution of 30,000, an AGC setting of 5×10^4 and a maximum injection time of 100 ms. Five of the 50 TMT batches were run on the Orbitrap Fusion mass spectrometer using the synchronous precursor selection-based (SPS)-MS3 method as previously described²¹.

TMT ROS/MAP database searches and protein quantification. All RAW files (1,200 RAW files generated from 50 TMT 10-plexes) were analyzed using the Proteome Discoverer suite (v.2.3, Thermo Fisher Scientific). MS2 spectra were searched against the UniProtKB human proteome database containing both Swiss-Prot and TrEMBL human reference protein sequences (90,411 target sequences downloaded on 21 April 2015), plus 245 contaminant proteins. The Sequest HT search engine was used and parameters were specified as follows: fully tryptic specificity, maximum of two missed cleavages, minimum peptide length of six, fixed modifications for TMT tags on lysine residues and peptide N-termini (+229,162932 Da) and carbamidomethylation of cysteine residues (+57,021464 Da), variable modifications for oxidation of methionine residues (+15,99492 Da) and deamidation of asparagine and glutamine (+0.984 Da), precursor mass tolerance of 20 ppm and a fragment mass tolerance of 0.05 Da for MS2 spectra collected in the Orbitrap (0.5 Da for the MS2 from the SPS-MS3 batches). Percolator was used to filter peptide spectral matches and peptides to an FDR <1%. Following spectral assignment, peptides were assembled into proteins and were further filtered based on the combined probabilities of their constituent peptides to a final FDR of 1%. In cases of redundancy, shared peptides were assigned to the protein sequence in adherence with the principles of parsimony. Reporter ions were quantified from MS2 or MS3 scans using an integration tolerance of 20 ppm with the most confident centroid setting.

PRM analysis. Peptides from brain digests used for the first three batches of the untargeted UPenn cohort analysis (equal to 1 µg protein digestion) were used for targeted analysis on an Orbitrap Lumos Tribrid Mass Spectrometer (Thermo Fisher Scientific) fitted with a Nanospray Flex ion source and coupled to a NanoAcuity liquid chromatography system (Waters). The tryptic peptides were resuspended in loading buffer (0.1% TFA, 500 ng µl⁻¹), and an external reference peptide mix (Promega) was spiked into the sample at the concentration of 0.5 pmol µl⁻¹. The solution (2 µl) was loaded onto a self-packed 1.9-µm ReproSil-Pur C18 (Dr Maisch) analytical column (New Objective, 50 cm × 75 µm inner diameter; 360 µm outer diameter) heated to 60 °C. The capillary temperature and spray voltage was set at 300 °C and 2.0 kV, respectively. Elution was performed over a 100-min gradient at a rate of 350 nL min⁻¹ with buffer B ranging from 1% to 32% (buffer A, 0.1% FA in water; buffer B, 0.1% FA in ACN). The column was then washed with 99% buffer B for 10 min and equilibrated with 1% B for 15 min. The mass spectrometer was set to collect in PRM mode using an inclusion peptide list (Supplementary Table 4). An additional full survey scan was collected to assess for possible interference. Full scans were collected at a resolution of 120,000 at 200 m/z with an AGC setting of 2×10^5 ion and a maximum ion transfer time of 50 ms. For PRM scans, the settings were: resolution at 30,000 at 200 m/z, AGC target of 1×10^5 ions, maximum ion transfer time of 50 ms, microscan count of 1, isolation width of 1.6 m/z and isolation offset of 0 m/z. A preoptimized normalized collision energy of 32% was used to obtain the maximal recovery of target product ions. The top 5–10 product ions from this collision energy optimization were used for downstream peptide quantification.

Peptide quantification. A spectral library was built using Skyline (v.4.2) based on tandem MS gathered from previous data-dependent acquisition methods. A Skyline template was then created to quantify the endogenous peptides. The template parameters were: centroided precursor mass analyzer, MS1 mass accuracy of 20 ppm; centroided product mass analyzer, MS/MS mass accuracy of 20 ppm, including all matching scans. All RAW files were imported and processed accordingly. The resulting extracted ion chromatograms of selected fragments were manually inspected and peak picking adjustments were made accordingly. The sum of all product ion peak areas was calculated in Skyline and extracted for further statistical analyses. The peak areas were normalized using the peak areas of external reference peptides. Raw peptide intensities are provided at <https://www.synapse.org/consensus>.

Selected reaction monitoring of ROS/MAP brain tissues. Samples were prepared for liquid chromatography (LC)-SRM analysis using a standard protocol described elsewhere²⁷. Briefly, on average ~20 mg of DLPFC brain tissue from each individual was homogenized in denaturation buffer. After denaturation with dithiothreitol, 400-µg protein aliquots were taken for further alkylation with iodoacetamide followed by digestion with trypsin as described. The digests were cleaned using C₁₈ solid phase extraction and 30-µl aliquots at 1 µg µl⁻¹ concentrations were mixed

with 30 µl of synthetic peptide mix. LC-SRM experiments were performed on a nanoACQUITY UPLC (Waters) coupled with a TSQ Vantage mass spectrometer (Thermo Fisher Scientific), with 2 µl of peptide injection for each brain sample. Buffer A was 0.1% FA in water and buffer B was 0.1% FA in 90% ACN. Peptide separations were performed on an Acquity UPLC BEH 1.7-µm C₁₈ column (75 µm inner diameter × 25 cm) at a flow rate 350 nL min⁻¹ using a gradient of 0.5% buffer B over 0 to 14.5 min, then 0.5% to 15% over 14.5 to 15.0 min, then 15% to 40% over 15 to 30 min and then 45% to 90% B over 30 to 32 min. The heated capillary temperature and spray voltage was set at 350 °C and 2.4 kV, respectively. Both the Q1 and Q3 were set as 0.7 full width half maximum (FWHM). A scan width of 0.002 m/z and a dwell time of 10 ms were used. All SRM data were analyzed using the Skyline software package. All data were manually inspected to ensure correct peak assignment and peak boundaries. The peak area ratios of endogenous light peptides and their heavy isotope-labeled internal standards (L/H peak area ratios) were automatically calculated by the Skyline software and the best transition without matrix interference was used for accurate quantification. Following homogenization of all tissues, small aliquots of protein from each of the samples was pooled, which were then digested and served as a global external pooled reference standard. Peptides generated from this pooled standard were scattered throughout the study (eight samples per 96-well plate) and were used to capture the technical variance that is due to sample preparation steps (except homogenization) and instrument measurements. The signal-to-noise ratio in quantification of each peptide was calculated as the ratio of variances across the human samples versus technical controls. Peptides with a signal-to-noise ratio <2 were excluded from further analysis. The peptide relative abundances were log₂ transformed and centered at the median. The abundance of endogenous peptides was quantified as a ratio to spiked-in synthetic peptides containing stable heavy isotopes. The 'light/heavy' ratios were log₂ transformed and shifted, such that median log₂-ratio was zero. Normalization adjusted for differences in the amount of protein among the samples. During normalization, the log₂-ratios were shifted for each sample to make sure the median was set at zero.

CSF samples. All participants from whom CSF samples were collected provided informed consent under protocols approved by the Institutional Review Board at Emory University. All patients received standardized cognitive assessments (including Montreal Cognitive Assessment) in the Emory Cognitive Neurology clinic, the Emory Goizueta Alzheimer's Disease Research Center (ADRC) and affiliated research studies (Emory Healthy Brain Study and Emory M'OVE-AD study). All diagnostic data were supplied by the ADRC and the Emory Cognitive Neurology Program. CSF was collected by lumbar puncture and banked according to 2014 ADC/NIA best practices guidelines. For patients recruited from the Emory Cognitive Neurology Clinic, CSF samples were sent to Athena Diagnostics and assayed for Aβ42, total Tau and phospho-Tau (CSF ADmark) using the INNOTEST assay platform. CSF samples collected from research participants in the ADRC, Emory Healthy Brain Study and M'OVE-AD were assayed using the INNO-BIA AlzBio3 Luminex assay. In total, there were two cohorts of CSF samples that were used in the proteomics studies. Cohort 1 contained CSF samples from 150 healthy controls and 147 mild cognitive impairment/AD patients. Cohort 2 included CSF obtained from three groups: 32 cognitively healthy, 31 AsymAD and 33 mild cognitive impairment/AD. Cases and healthy individuals with AsymAD were defined using established biomarker cutoff criteria for AD for each assay platform^{68,69}. Cohort information is provided in Supplementary Table 1.

CSF protein digestion. To generate peptides, all crude CSF samples were digested with LysC and trypsin. Briefly, 20 µl of CSF from each sample was reduced and alkylated with 0.4 µl of 0.5 M tris-2-(carboxyethyl)-phosphine and 2 µl of 0.4 M chloroacetamide with heating at 90 °C for 10 min, followed by a 15-min water bath sonication. The samples were then further denatured by the addition of 67.2 µl of 8 M urea buffer (8 M urea, 100 mM NaHPO₄, pH 8.5) and digested overnight with 1.9 µg of LysC (Wako) (1:10 enzyme to protein ratio according to the highest amount of sample). Following LysC digestion, the samples were diluted to 1 M urea using 50 mM ammonium bicarbonate. The same amount of trypsin (Promega) was then added (1:10 enzyme to protein ratio) and digestion was carried out for another 12 h. After trypsin digestion, peptide solutions were acidified with a 1% TFA and 10% FA solution to a final concentration of 0.1% TFA and 1% FA. Peptides were desalted with a 30-mg C18 HLB column (Waters) and eluted in 1 ml of 50% ACN. Aliquots (120 µl) from cohort 1 (*n* = 297) or cohort 2 (*n* = 96) samples were pooled together and split into equal volume aliquots (880 µl) for use as the GIS for TMT labeling. All samples and GIS were dried using a SpeedVac.

TMT boost channel. Signals of low-abundant proteins in the TMT 11-plex were amplified using a boost channel, as previously described¹⁷⁰. A pooled CSF sample was created separately for each cohort by combining 50 µl from each sample in cohort 1 or cohort 2 into a pool for each cohort. Abundant proteins were removed using the High Select Top14 Abundant Proteins Depletion Resin (Thermo Fisher Scientific A36372BR) according to the manufacturer's protocol, using a CSF-to-resin volume ratio of 1:1 and an incubation time of 15 min. After immunodepletion, protein concentrations were determined by bicinchoninic acid. Proteins were then reduced and alkylated (10 mM tris-2-(carboxyethyl)-phosphine,

40 mM chloroacetamide) for 10 min at 90 °C. The samples were then subjected to bath sonication for 15 min and dried under vacuum in a SpeedVac. The immunodepleted pooled samples were resuspended in 6 M urea buffer (6 M urea, 75 mM NaHPO₄, pH 8.5) at half the volume of the pooled sample before evaporation. Samples were digested overnight with LysC at an enzyme to protein ratio of 1:10. The following day, samples were diluted with 50 mM ammonium bicarbonate to reduce the urea concentration to 1 M and trypsin (Promega) was added (1:10 enzyme to protein ratio). Digestion was allowed to proceed for 12 h. Peptides were then desalted using a 200 mg C18 Sep-Pak column and the eluate was dried using a SpeedVac. Aliquots (600 µg) of the immunodepleted pooled CSF samples were separately dissolved in 100 mM TEAB buffer (625 µl) and labeled with 5 mg of TMT 126 channel reagent (cohort 1 lot TF266326, cohort 2 lot SG253447, Thermo Fisher Scientific) in anhydrous ACN (256 µl). The reactions were allowed to proceed for 1 h and were subsequently quenched by adding 5% hydroxylamine (50 µl) and incubating for 15 min. The 126 channel was then added to the other channels, as described below.

TMT labeling of individual and GIS CSF samples. All samples, including the GIS, were labeled with the 10-plex TMT kit plus an additional channel, for a total of 11 TMT channels (cohort 1 lot TG273545 for 10-plex, TG273555 for channel 131 C; cohort 2 lot SI258088 for 10-plex, SJ258847 for channel 131 C, Thermo Fisher Scientific). Samples were grouped into batches as shown in Supplementary Table 1. The TMT labeling kit was equilibrated to room temperature and dissolved in anhydrous ACN (256 µl). The samples were reconstituted in 100 mM TEAB buffer (50 µl) and mixed with 0.4 mg (20.5 µl) of the corresponding labeling reagent. The labeling reactions were allowed to proceed for 1 h and were subsequently quenched with 5% hydroxylamine (4 µl). For each TMT batch, labeled peptides from nine channels (127 N, 128 N, 128 C, 129 N, 129 C, 130 N, 130 C, 131, 131 C) were mixed, desalted using a 100-mg C18 Sep-Pak column and dried using a SpeedVac. The immunodepleted pooled sample labeled with the 126 channel (boost channel) was then added to each nine-channel TMT mixture at a ratio of 50:1 pooled to individual CSF sample by original volume:volume before evaporation. The sample mixtures were desalted using a 200-mg C18 Sep-Pak column and dried using a SpeedVac.

MS analysis of CSF. All samples were resuspended in an equal volume of loading buffer (0.1% FA, 0.03% TFA, 1% ACN). Peptide eluents were separated on a self-packed C18 (1.9 µm, Dr Maisch, Germany) fused silica column (25 cm × 75 µM internal diameter, New Objective) by an Easy-nLC system (Thermo Fisher Scientific) and monitored on an Orbitrap Fusion Lumos mass spectrometer (Thermo Fisher Scientific) interfaced with a high-field asymmetric waveform ion mobility spectrometry Pro. Sample elution was performed over a 180-min gradient (buffer A, 0.1% FA in water; buffer B, 0.1% FA in 80% ACN) with flow rate at 225 nL min⁻¹. The gradient was from 1% to 8% buffer B over 3 min, then from 8% to 40% over 160 min, then from 40% to 99% over 10 min and then held at 99% B for 10 min. The mass spectrometer was set to acquire data in positive-ion mode using data-dependent acquisition and three (-50, -65 and -85 V) different compensation voltages. Data were acquired at each compensation voltage for 1 s during each cycle. Each cycle consisted of one full scan followed by as many MS2 and MS3 scans as possible within a 1-s timeframe. The full scan was performed with an m/z range of 450–1,500 at 120,000 resolution (at 200 m/z) with an AGC setting of 4 × 10⁵ and maximum injection time of 50 ms. The collision-induced dissociation MS/MS scans were collected in the ion trap with an isolation window of 0.7 m/z, a collision energy of 35%, AGC setting of 1 × 10⁴ and a maximum injection time of 50 ms. The top ten product ions were subjected to higher energy collision-induced dissociation SPS-MS3 as previously described²¹. For SPS-MS3 scans the isolation window was set to 2 m/z, the resolution to 50,000, the AGC to 1 × 10⁵ and the maximum injection time to 105 ms. For both cohorts, a single preliminary run of TMT batch 1 using the above parameters was used to create a target inclusion list of peptides that specifically excluded those from the top 15 most abundant proteins. This inclusion list was used for all TMT batches in cohort 1 (*n* = 38) and in cohort 2 (*n* = 12).

Database searches and protein quantification of CSF. All RAW files were analyzed using the Proteome Discoverer Suite (v.2.3, Thermo Fisher Scientific). MS/MS spectra were searched against the UniProtKB human proteome database (downloaded in April 2015 with 90,411 total sequences). The Sequest HT search engine was used to search the RAW files, with search parameters specified as follows: fully tryptic specificity, maximum of two missed cleavages, minimum peptide length of six, fixed modifications for TMT tags on lysine residues and peptide N-termini (+229.162932 Da) and carbamidomethylation of cysteine residues (+57.02146 Da), variable modifications for oxidation of methionine residues (+15.99492 Da), serine, threonine and tyrosine phosphorylation (+79.966 Da) and deamidation of asparagine and glutamine (+0.984 Da), precursor mass tolerance of 20 ppm and a fragment mass tolerance of 0.6 Da. Percolator was used to filter peptide spectral matches and peptides to an FDR <1%. Following spectral assignment, peptides were assembled into proteins and were further filtered based on the combined probabilities of their constituent peptides to a final FDR of 1%. In cases of redundancy, shared peptides were assigned to the protein

sequence in adherence with the principles of parsimony. Reporter ions were quantified from MS3 scans using an integration tolerance of 20 ppm with the most confident centroid setting, as previously described²¹.

Controlling for batch-specific variance. We implemented a median polish algorithm for removing technical variance (for example, due to tissue collection, cohort or batch effects) from a two-way abundance-sample data table as originally described by Tukey²¹. The algorithm is fully documented and available as an R function that can be downloaded from <https://github.com/edammer/TAMPOR>. The algorithm implements iterations of the below equation, where batch and cohort are interchangeable.

$$\frac{\text{abundance}}{\text{median(ALL SAMPLES)/batch}} \times \frac{\text{grand median}}{\text{median} \left(\left\{ \frac{\text{abundance}}{\text{median(ALL SAMPLES)/batch}} | \text{all samples from batch} \right\} \right)} \quad (1)$$

Briefly, Equation 1 is applied to each protein measurement (LFQ or TMT reporter abundance) across all samples individually where the first term represents batch-wise median-centered abundance and the second term is a batch-specific normalization factor comprised of the grand median of all batch-specific medians, divided by the appropriate batch-specific median of median-centered abundances. The data matrix is then log₂-transformed and each log₂(ratio) is adjusted by subtraction of sample (column)-wise median log₂(ratio) for all proteins. Then, ratios are anti-logged and multiplied by the protein (row)-wise median of all samples used for Equation 1 term 1 denominator, extracted before Equation 1 was executed. This process is iterated until convergence. The use of median polish ensures that the reduction of variance is robust to outliers, while the overall algorithm preserves biological variance, given that batches have been randomized to avoid confounding batch with diagnosis or other biological traits. Before matrix assembly for the consensus analysis, intracohort batch effects were first removed in the MSSB (batch correction with 166 case samples across seven batches) and Banner (batch correction with 178 case samples across four batches) cohorts. All remaining batch corrections restricted the first term denominator to global pooled (within cohort) standard sample abundances and the second term used all individual case samples. Following removal of intracohort batch effects in MSSB and Banner, all samples were processed jointly with the algorithm in the same sample-protein matrix to capture biological variance across all samples in all four cohorts (ACT, Banner, BLSA and MSSB) for the consensus analysis. The above algorithm was applied to a matrix in which proteins that had ≥50% missing values were removed. For the consensus LFQ network, 450 case samples (three ACT outliers were removed before inclusion, as described below) classified as control, AsymAD or AD by our unified criteria (see case classification methods above) were considered as 'all samples' for denominators in Equation 1. All remaining batch corrections, listed as follows, restricted the first term denominator to global pooled (within cohort) standard sample abundances and the second term used all individual case samples.

For ROS/MAP 50-batch TMT protein abundances, there were two pooled GIS channels in each TMT batch (*n* = 64) and 400 individual case samples (non-internal standard samples). For the Hopkins aging cohort (84 case samples), global pool mixture samples (three each per three batches) were used for the first term denominator, with the second term using all nonglobal pool mixture samples. For the UPenn PRM analysis (three batches, 114 case samples and nine pooled controls), data were likewise batch corrected using three global pool mixture samples per batch for the first term denominator and all within-batch nonpooled samples for the second term. UPenn LFQ data (ten batches, 330 case samples and 29 control pools) were similarly batch corrected as described. CSF 96-case and 300-case TMT normalized abundances were also batch corrected using the above algorithm, with Equation 1 first term denominator restricted to global pooled (within cohort) standard sample abundances, whereas the second term used all individual non-internal standard case samples.

Regression for covariates and outlier removal. No imputation of missing values was performed in any cohort. Nonparametric bootstrap regression was performed separately in each cohort by subtracting the trait of interest (age at death, sex or PMI) times the median estimated coefficient from 1,000 iterations of fitting for each protein in the cohort-specific log₂(abundance) matrix. Ages at death used for regression were uncensored. Case status/diagnosis was also explicitly modeled (protected) in each regression. Following regression of each individual cohort, we assessed whether any cohort-specific tissue dissection bias was present by performing a Spearman rank correlation of traits including age, sex, PMI and white matter markers to the top five PCs of log₂(abundance). Network outlier case samples were not considered in the PCs and were identified before PC analysis using Oldham's 'SampleNetworks' v.1.06 R script²² as previously published²² using a threefold s.d. cutoff of Z-transformed sample connectivity. The Spearman rank correlation was performed before correction of cohort-specific batch effects as described above and after intracohort batch correction of MSSB and Banner cohorts. All four cohorts were confirmed to have no significant PC correlation to age, sex or PMI; however, ACT was observed to have a first PC significantly correlated (average rho = 0.94) to protein abundance of white matter markers

identified previously as oligodendrocyte coexpression network hubs¹⁷. These markers were BCAS1, SIRT2, MBP and MAG. This white matter PC represented 27% of variance in the ACT cohort, whereas the white matter marker-correlated PC represented 7 to 12% variance in the other three cohorts. To adjust for white matter variance in ACT, we applied a second round of bootstrap regression to the 62 non-outlier ACT case sample log₂(abundances), using white matter PC as a regression covariate and subtracted 28% of white matter marker-correlated variance to achieve a final variance of 12% after recalculation of the top five PCs. Abundance data for the 450 case samples were then assembled into a matrix of 3,334 proteins and cross-cohort batch correction by median polish was performed as described above. Finally, network outlier detection was performed as described above, which removed 31 of 450 cases from consideration in the four-cohort consensus network and differential abundance analyses. All outliers are listed in Supplementary Table 2. In all other cohorts that were not combined for the consensus network analysis, batch correction was performed first, followed by outlier removal, followed by removal of proteins with $\geq 50\%$ missing values and then regression of age, sex and PMI before coexpression network and differential abundance analyses. In the Hopkins aging cohort, age was not considered as a trait for regression. In the CSF cohorts, only age at time of collection and sex were considered for regression.

Differential expression analysis. Differentially expressed proteins were found using one-way ANOVA followed by Tukey's comparison post hoc test across control, AsymAD and AD cases. Significantly altered proteins with corresponding *P* value are provided in Supplementary Tables 2 and 5 for consensus AD network proteins and astrocyte/microglial phenotype proteins, respectively. Differential expression is presented as volcano plots that were generated with the ggplot2 package in R v.3.5.2.

Protein correlations with aging. Protein expression levels for all 2,756 proteins measured in the aging cohort with fewer than 50% missing values were correlated with age at death using the bicor function, after regression for sex and PMI. In addition to bicor rho, the Student's *P* value for significance of the correlation, FDR (*q* value) and signed *z* score for the correlation were calculated. The CSGene database of cellular senescence genes⁷³ was cross-referenced with protein data to annotate proteins involved in cellular senescence. This information is provided in Supplementary Table 3, along with differences between AD, control or AsymAD for the same proteins in the consensus network and their corresponding consensus network module relationships. Individual correlations for proteins in the consensus network to all traits provided in Supplementary Fig. 1 are provided online at <https://www.synapse.org/consensus>.

Weighted correlation network analysis. We used the WGCNA algorithm for our network analysis pipeline, as previously described²². A weighted protein coexpression network for the four-cohort consensus data was generated using the 3,334 log₂ protein abundance \times 419 case-sample matrix that had undergone covariate and batch correction as described above. The WGCNA::blockwiseModules() function was used with the following settings: soft threshold power $\beta = 5.5$, deepSplit = 4, minimum module size of 14, merge cut height of 0.07, mean TOM denominator, a signed network with partitioning about medioids respecting the dendrogram, a minimum *k_{ME}* to remain in a module of 0.30 and a reassignment threshold of *P* < 0.05. Specifically, we calculated pairwise biweight mid-correlations (bicor, a robust correlation metric) between each protein pair and transformed this correlation matrix into a signed adjacency matrix. The connection strength of components within this matrix was used to calculate a topological overlap matrix, which represents measurements of protein expression pattern similarity across cohort samples constructed on the pairwise correlations for all proteins within the network. Hierarchical protein correlation clustering analysis by this approach was conducted using 1-TOM, and initial module identifications were established using dynamic tree cutting as implemented in the WGCNA::blockwiseModules() function. Module eigenproteins were defined, which represent the most representative abundance value for a module and which explain covariance of all proteins within a module¹⁶. Pearson correlations between each protein and each module eigenprotein were performed; this module membership measure is defined as *k_{ME}*. After the initial network construction, 18 modules consisting of 14 or more proteins were detected. Given high *k_{ME}* similarity between some modules, we used the WGCNA::moduleMergeUsingKME() function to reduce the number of modules to 13, with the following parameters: percentage of module members checked for *k_{ME}* overlap of 50% (threshPercent = 50), threshold for merging modules with high common *k_{ME,intramodule}* of 25% (mergePercent = 25) and all other parameters default for the function. After module merging, module eigenproteins (MEs) and signed *k_{ME}* values were recalculated with the WGCNA::moduleEigengenes() and WGCNA::signedKME() functions, respectively. Finally, we 'cleaned' the network of assignments with aberrant *k_{ME}* (as WGCNA clustering into modules and merging of those modules use hybrid approaches not solely dependent on *k_{ME}*) by applying the following algorithm: remove module members with *k_{ME,intramodule}* < 0.28, then check all gray (unclustered) proteins for *k_{ME}* > 0.35 and assign to the module with the highest *k_{ME,intramodule}*. For BLSA precuneus, Mayo temporal cortex and ROS/MAP cohorts, we confirmed that

they built networks using the pipeline described above, including batch correction, outlier removal and age, sex and PMI regression. Network building was employed without module merging. The blockwiseModules function for ROS/MAP used a power of 10 and minimum module size of 30 (11,225 proteins in 323 nonexcluded and non-outlier case samples); for BLSA precuneus, it used a power of 8 and minimum module size of 4 (3,348 proteins in 46 case samples); and for Mayo, it used a power of 5 and minimum module size of 14 (3,951 proteins in 107 case samples). For analysis of sex effects on the consensus network, the identical cases and analysis pipeline as described above were used to build the consensus network, except that covariance due to sex was not removed by regression before WGCNA analysis.

Network preservation. We used the WGCNA::modulePreservation() function to assess network module preservation across cohorts. We also used this function to assess the effect of missing values on the consensus network. *Z_{summary}* composite preservation scores were obtained using the consensus network as the template versus each other cohort or missing value threshold tested, with 500 permutations. Random seed was set to 1 for reproducibility and the quickCor option was set to 0. We also assessed network module preservation using synthetic eigenproteins. Briefly, protein module members in the consensus network template with a *k_{ME,intramodule}* among the top 20th percentile were assembled into a synthetic module in each target cohort and synthetic modules with at least four members were used to calculate synthetic weighted eigengenes representing the variance of all members in the target network across case samples via the WGCNA::moduleEigengenes() function. Statistics and correlation scatter-plots involving target cohort traits were then calculated and visualized.

Gene ontology and cell type marker enrichment analyses. To characterize differentially expressed proteins and co-expressed proteins based on GO annotation, we used GO Elite v.1.2.5 as previously published²², with pruned output visualized using an inhouse R script. Cell type enrichment was also investigated as previously published⁷². Astrocyte subtype markers were obtained from Zamanian et al.²⁶. Microglia subtype markers were obtained from Rangaraju et al.²⁷.

GWAS module association. To determine whether any protein products of GWAS targets were enriched in a particular module, we used the single nucleotide polymorphism summary statistics from the International Genomics of Alzheimer's Project (http://www.pasteur-lille.fr/en/recherche/u744/igap/igap_download.php) to calculate the gene level association value using MAGMA²⁵, as previously described¹⁷. *APOE* was added to the gene list and assigned a $-\log P$ value of 50, given its known strong association with AD. *ApoE* did not fall within a network module and therefore did not influence the reported module enrichment results. Similar analyses were performed with GWAS candidates for schizophrenia and autism spectrum disorder. These GWAS datasets were provided and downloaded from the Psychiatric Genomics Consortium (<http://www.med.unc.edu/pgc/downloads>).

Curation of AD mouse model purified glial transcriptomic and proteomic data. Orre et al.³² microarray data files (*n* = 11; files last updated on 20 July 2015) were downloaded from the NCBI Gene Expression Omnibus datasets website (identifier GSE74615). The data, consisting of 22 samples, were normalized and centered based on limma R package user guidelines with backgroundCorrect method = 'normexp' and normalizeBetweenArrays method = 'quantile'. Transcripts with signal at least 110% of the 95th percentile of all normalized red negative control spots on the arrays in at least 4 of 22 samples were considered as expressed above noise in at least one cell type (*n* = 28,157 gene transcripts across *N* = 14 purified microglial measurements and *N* = 8 purified astrocyte measurements). WGCNA collapseRows function was used to handle multiple probe mappings to any gene, with probe selection method = 'maxRowVariance'. Grubman et al.³³ peptide-level total peak area data for $XO4^+$ (amyloid- β plaque phagocytosing) and $XO4^-$ (amyloid- β plaque nonphagocytosing) acutely purified microglia from AD and wild-type mice, respectively, were summed and log₂-transformed to achieve protein-level data for 94 gene product proteins. Grubman et al. mRNA-level measurements were obtained directly and used without further processing.

Statistics. All statistical analyses were performed in R (v.3.5.2). Box plots represent the median, 25th and 75th percentiles and whiskers with staples represent measurements to the 5th and 95th percentiles of non-outlier samples; outlier samples are plotted beyond these whiskers as open circles. Correlations were performed using the biweight midcorrelation function as implemented in the WGCNA R package. Comparisons between two groups were performed by Student's *t*-test. Comparisons among three or more groups were performed with Kruskal-Wallis nonparametric ANOVA or standard ANOVA with Tukey or Dunnnett post hoc pairwise comparison of significance. *P* values were adjusted for multiple comparisons by FDR correction where indicated. The *t*-distributed stochastic neighbor embedding analysis was implemented with R package Rtsne, as previously published¹⁷. Module membership graphs were generated using the igraph R package as previously described^{17,74}.

Reporting Summary. Further information on research design is available in the Nature Research Reporting Summary linked to this article.

Data availability

All raw data, case traits and analyses (differential and coexpression) related to this manuscript are available at <https://www.synapse.org/consensus>. The results published here are in whole or in part based on data obtained from the AMP-AD Knowledge Portal (<https://adknowledgeportal.synapse.org/>). The AMP-AD Knowledge Portal is a platform for accessing data, analyses and tools generated by the AMP-AD Target Discovery Program and other programs supported by the National Institute on Aging to enable open-science practices and accelerate translational learning. The data, analyses and tools are shared early in the research cycle without a publication embargo on secondary use. Data are available for general research use according to the following requirements for data access and data attribution (<https://adknowledgeportal.synapse.org/#/DataAccess/Instructions>). ROS/MAP resources can be requested at www.radc.rush.edu.

Code availability

The algorithm used for batch correction is fully documented and available as an R function, which can be downloaded from <https://github.com/edammer/TAMPOR>.

References

57. O'Brien, R. J. et al. Neuropathologic studies of the baltimore longitudinal study of aging (BLSA). *J. Alzheimers Dis.* **18**, 665–675 (2009).
58. Beach, T. G. et al. Arizona study of aging and neurodegenerative disorders and brain and body donation program. *Neuropathology* **35**, 354–389 (2015).
59. Bennett, D. A. et al. Religious orders study and rush memory and aging project. *J. Alzheimers Dis.* **64**, S161–S189 (2018).
60. Braak, H. & Braak, E. Neuropathological staging of Alzheimer-related changes. *Acta Neuropathol.* **82**, 239–259 (1991).
61. Ince, P. G., Ince, P. G., Lowe, J. & Shaw, P. J. Review. *Neuropathol. Appl. Neurobiol.* **24**, 104–117 (1998).
62. Balsis, S., Benge, J. F., Lowe, D. A., Geraci, L. & Doody, R. S. How do scores on the ADAS-cog, MMSE, and CDR-SOB correspond? *Clin. Neuropsychol.* **29**, 1002–1009 (2015).
63. Cox, J. et al. Accurate proteome-wide label-free quantification by delayed normalization and maximal peptide ratio extraction, termed MaxLFQ. *Mol. Cell Proteomics* **13**, 2513–2526 (2014).
64. Luber, C. A. et al. Quantitative proteomics reveals subset-specific viral recognition in dendritic cells. *Immunity* **32**, 279–289 (2010).
65. Mertins, P. et al. Reproducible workflow for multiplexed deep-scale proteome and phosphoproteome analysis of tumor tissues by liquid chromatography–mass spectrometry. *Nat. Protoc.* **13**, 1632–1661 (2018).
66. Wingo, T. S. et al. Integrating next-generation genomic sequencing and mass spectrometry to estimate allele-specific protein abundance in human brain. *J. Proteome Res.* **16**, 3336–3347 (2017).
67. Petyuk, V. A., Qian, W. J., Smith, R. D. & Smith, D. J. Mapping protein abundance patterns in the brain using voxelation combined with liquid chromatography and mass spectrometry. *Methods* **50**, 77–84 (2010).
68. Hulstaert, F. et al. Improved discrimination of AD patients using β-amyloid(1–42) and tau levels in CSF. *Neurology* **52**, 1555–1562 (1999).
69. Shaw, L. M. et al. Cerebrospinal fluid biomarker signature in Alzheimer's disease neuroimaging initiative subjects. *Ann. Neurol.* **65**, 403–413 (2009).
70. Yi, L. et al. Boosting to amplify signal with isobaric labeling (BASIL) strategy for comprehensive quantitative phosphoproteomic characterization of small populations of cells. *Anal. Chem.* **91**, 5794–5801 (2019).
71. Tukey, J. W. *Exploratory Data Analysis* (Addison-Wesley, 1977).
72. McKenzie, A. T. et al. Multiscale network modeling of oligodendrocytes reveals molecular components of myelin dysregulation in Alzheimer's disease. *Mol. Neurodegener.* **12**, 82 (2017).
73. Zhao, M., Chen, L. & Qu, H. CSGene: a literature-based database for cell senescence genes and its application to identify critical cell aging pathways and associated diseases. *Cell Death Dis.* **7**, e2053 (2016).
74. Umoh, M. E. et al. A proteomic network approach across the ALS-FTD disease spectrum resolves clinical phenotypes and genetic vulnerability in human brain. *EMBO Mol. Med.* **10**, 48–62 (2018).

Acknowledgements

We are grateful to those who agreed to donate their brains and CSF for research and who participated in the described observational studies. This study was supported by the following National Institutes of Health funding mechanisms: R01AG053960, R01AG057911, R01AG061800, RF1AG057471, RF1AG057470, R01AG061800, R01AG057911, R01AG057339, U01AG061357, P50AG025688, RF1AG057470, RF1AG051633, P30AG10161, R01AG15819, R01AG17917, U01AG61356, R01AG056533, K08NS099474, U01AG046170, RF1AG054014, RF1AG057440, R01AG057907, U01AG052411, P30AG10124, U01AG046161, R01AG050631, R01AG053960, R01AG057339, U01AG061357, P50AG005146, U24NS072026 and P30AG19610. The study was also supported in part by the intramural program of the National Institute on Aging (NIA).

Author contributions

E.C.B.J., E.B.D., D.M.D., L.P., M.Z., A.G., V.A.P. and N.T.S. designed experiments; D.M.D., L.P., M.Z., L.Y., A.G. and V.A.P. carried out experiments; E.C.B.J., E.B.D., M.Z., V.A.P. and N.T.S. analyzed data; D.M.D., L.P., L.A.H., B.W., J.C.T., M.T., T.J.M., E.B.L., J.Q.T., T.G.B., E.M.R., V.H., M.W., E.S., B.Z., D.W.D., N.E.-T., T.E.G., V.A.P., P.L.D.J., D.A.B., T.S.W., S.R., I.H. and J.M.S. provided advice on the interpretation of data; E.C.B.J. wrote the manuscript with input from co-authors; J.C.T., T.J.M., J.Q.T., T.G.B., V.H., M.W., D.W.D., D.A.B. and I.H. provided tissue samples; A.I.L., J.J.L. and N.T.S. supervised the study. All authors approved the final manuscript.

Competing interests

The authors declare no competing interests.

Additional information

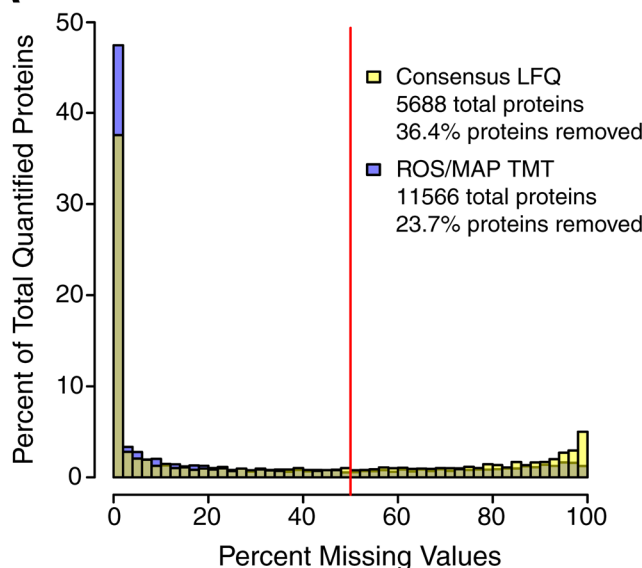
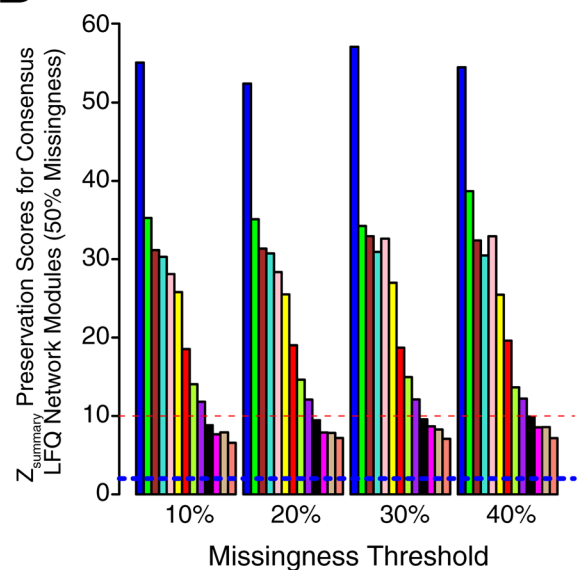
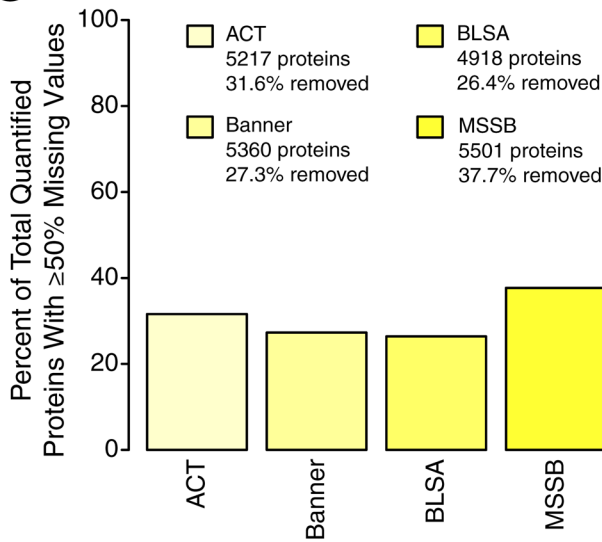
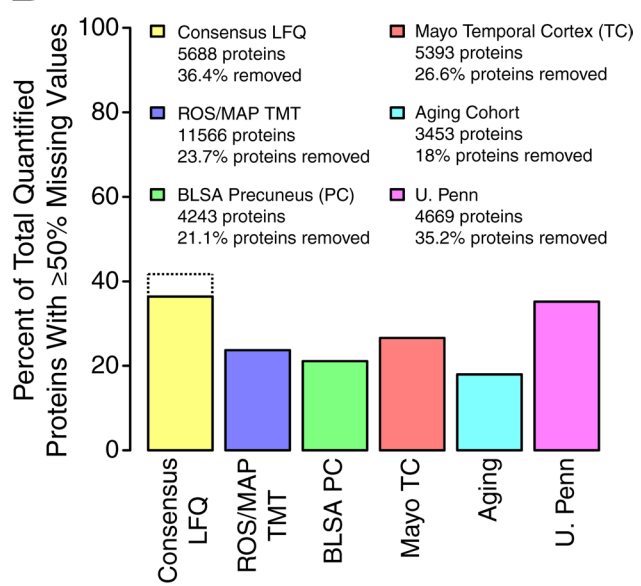
Extended data is available for this paper at <https://doi.org/10.1038/s41591-020-0815-6>.

Supplementary information is available for this paper at <https://doi.org/10.1038/s41591-020-0815-6>.

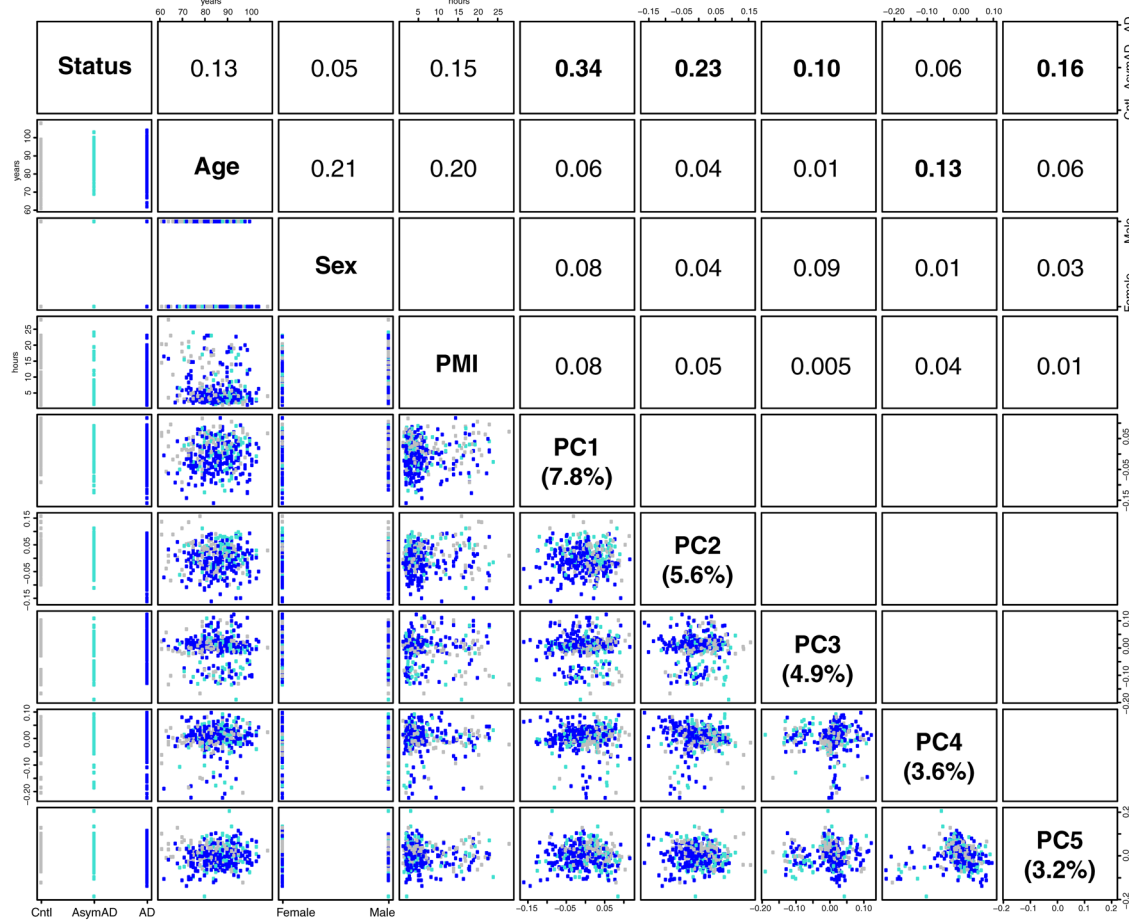
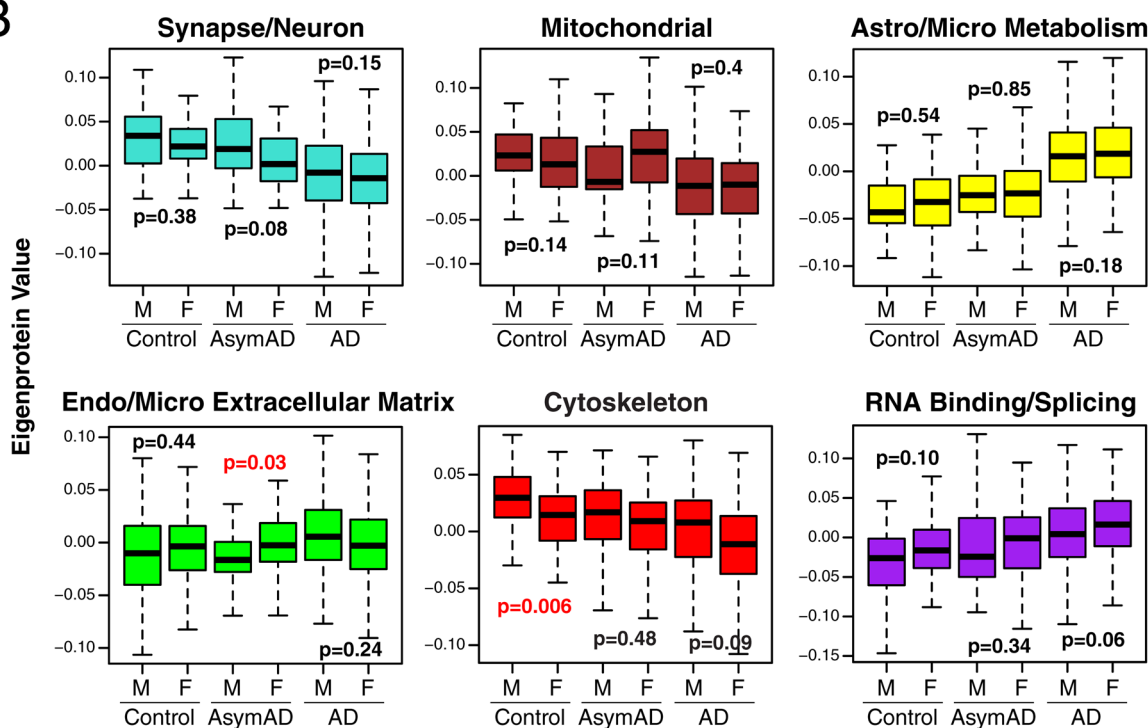
Correspondence and requests for materials should be addressed to E.C.B.J., A.I.L. or N.T.S.

Peer review information Kate Gao was the primary editor on this article, and managed its editorial process and peer review in collaboration with the rest of the editorial team.

Reprints and permissions information is available at www.nature.com/reprints.

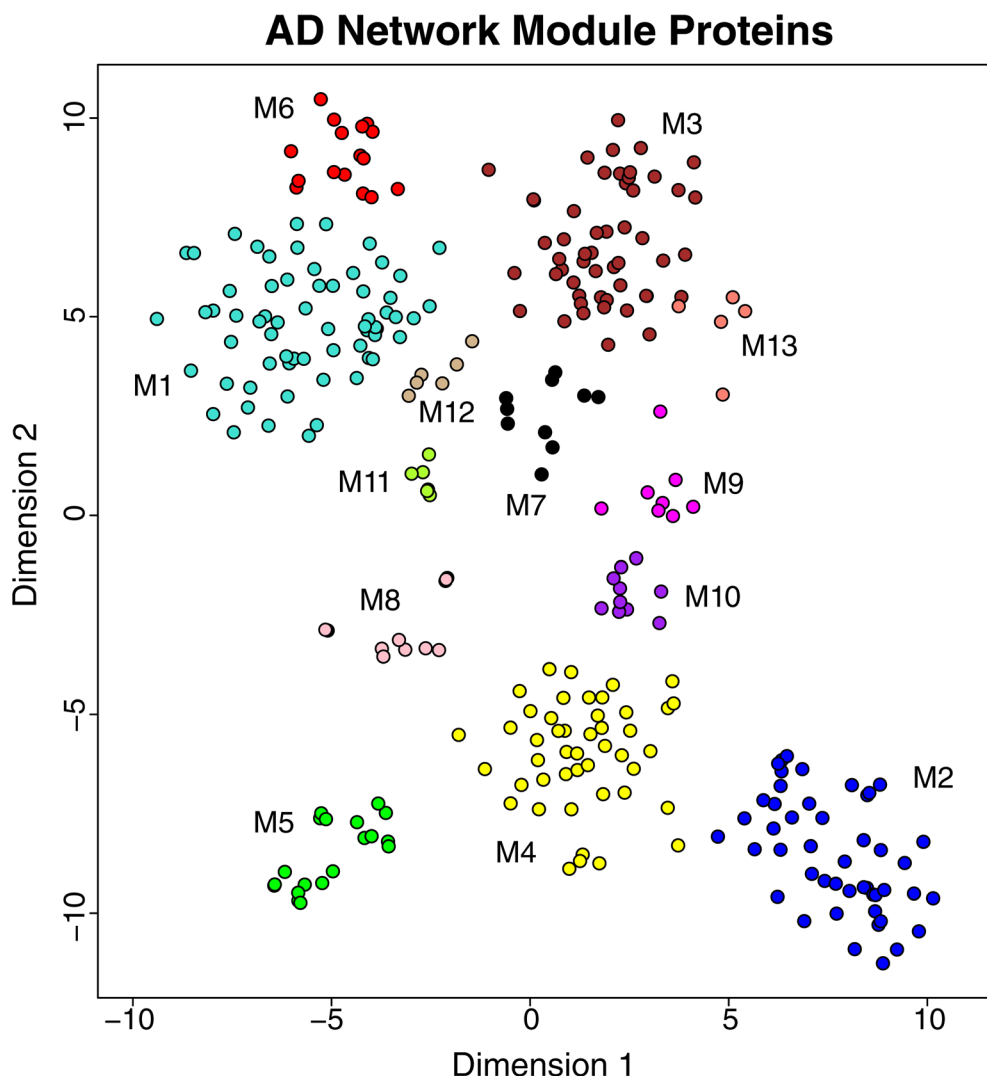
A**B****C****D**

Extended Data Fig. 1 | Analysis of Missing Protein Quantitative Measurements and their Effect on the AD Network. **a-d**, The percentage of quantified proteins with a given level of missing quantitative measurements was analyzed for both the consensus LFQ and ROS/MAP TMT networks (**a**). Each bar represents a bin of 2%. The red line indicates the 50% missing measurement threshold used in this study. The total number of quantified proteins for each dataset, and the percentage of quantified proteins removed due to $\geq 50\%$ missing measurements prior to construction of the respective protein networks, is provided in the legend. **b**, The effect of missing value threshold on AD network modules. The AD network was constructed using different allowed levels of missing protein measurements. Preservation of AD network modules (50% missingness threshold) in each network generated using a more stringent threshold (10–40% missingness) was assessed by Z_{summary} score. Module preservation Z_{summary} was calculated as described by Langfelder et al.⁷⁴ The dashed blue line indicates a Z_{summary} score of 1.96, or FDR q value <0.05 , above which module preservation was considered statistically significant. The dashed red line indicates a Z_{summary} score of 10, or FDR q value $\sim 1e^{-23}$, above which module preservation was considered highly statistically significant. Each module is color coded as shown in Fig. 1. Module memberships are provided in Supplementary Table 2. **c**, Percentage of total quantified proteins with $\geq 50\%$ missing measurements in each cohort used for the AD consensus network. The total number of quantified proteins, and the percentage removed by applying the $\geq 50\%$ missingness threshold, is provided in the legend for each cohort. **d**, Percentage of total quantified proteins with $\geq 50\%$ missing measurements in each cohort used in this study. The total number of quantified proteins, and the percentage removed by applying the $\geq 50\%$ missingness threshold, is provided in the legend for each cohort. For the consensus LFQ cohort, the dotted line indicates the percent removed (41.3%) when missingness is controlled separately in each cohort prior to combination for construction of the AD network, as was done in this study. The solid bar is provided for direct method comparison to other cohorts used in the study. LFQ, label-free quantitation; TMT, tandem-mass tag; BLSA, Baltimore Longitudinal Study of Aging; Banner, Banner Sun Health Research Institute; MSSB, Mount Sinai School of Medicine Brain Bank; ACT, Adult Changes in Thought Study; ROS/MAP, Religious Orders Study and Memory and Aging Project; PC, precuneus; TC, temporal cortex.

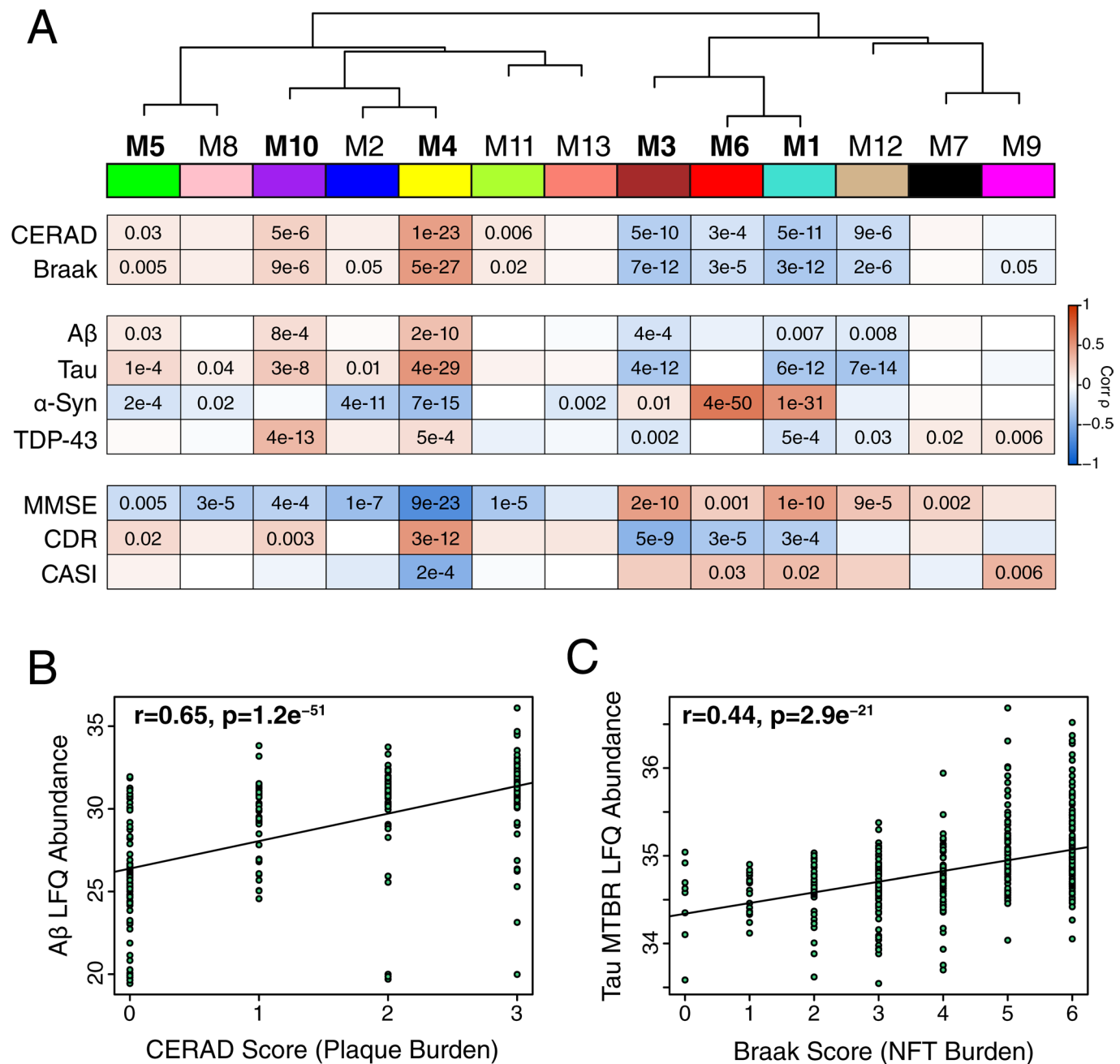
A**B**

Extended Data Fig. 2 | See next page for caption.

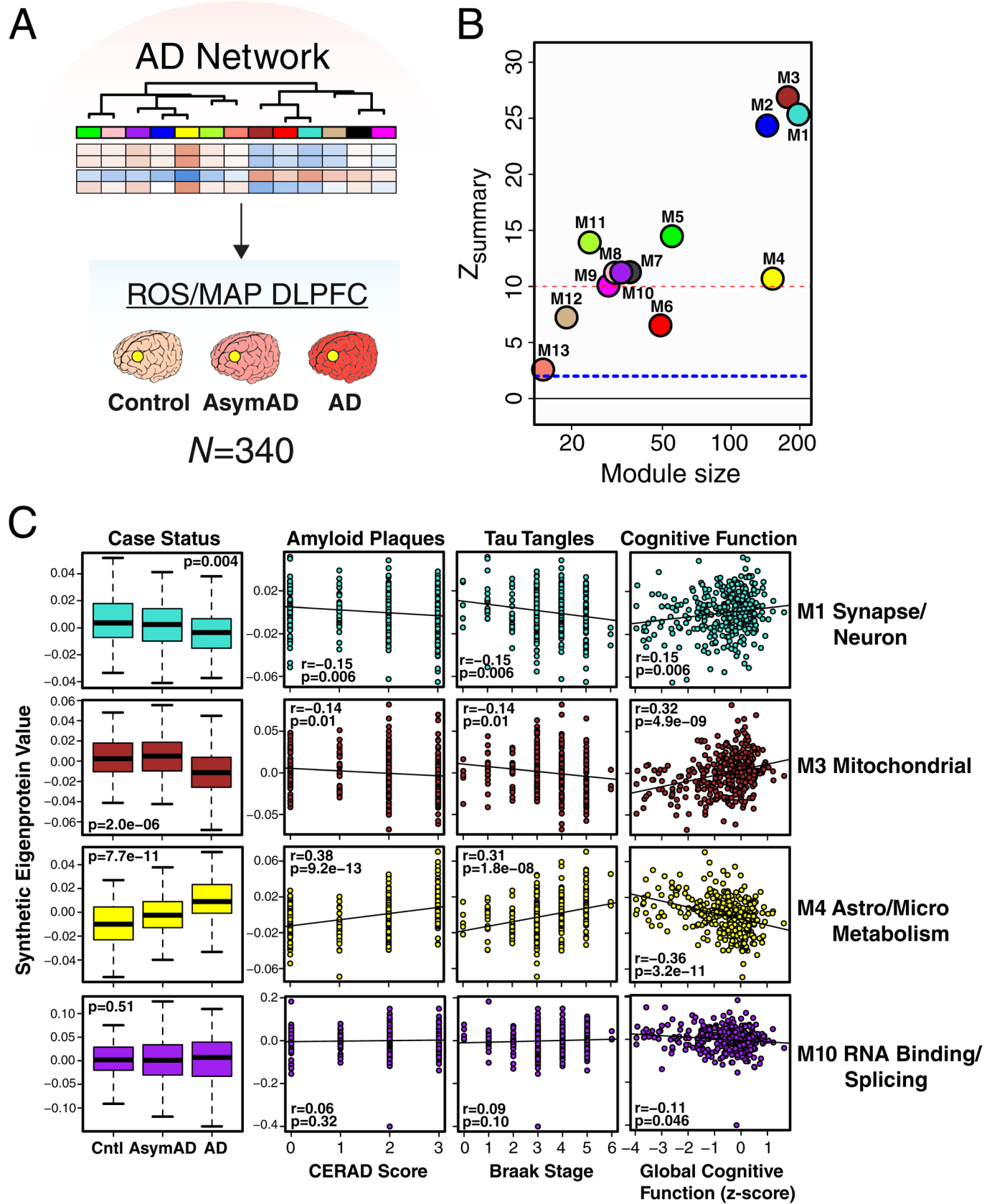
Extended Data Fig. 2 | Covariate Effects on AD Network Protein Quantitative Values and Modules. **a,b**, Principal component analysis was performed on AD network protein quantitative values after batch correction but prior to regression for age, sex, and post-mortem interval (PMI) covariates ($n=418$ case samples after network connectivity outlier removal) (**a**). Correlation values between case status (control, AsymAD, or AD), age, sex, PMI, and the first five principal components of the data are shown. The covariate most strongly correlated to each principal component is highlighted in bold. The percentage of variance in the data explained by each principal component is given in parentheses. (**b**), Effects of sex on AD network modules shown in Fig. 1c. The AD network was built without regression for sex, and module eigenprotein levels were compared between male and female sex for each case group ($n=123$ AD, 54 AsymAD, 44 control females; $n=103$ AD, 45 AsymAD, 49 control males). Statistically significant differences are highlighted in red. Correlations were performed using Spearman's rank correlation. Differences in protein levels were assessed by Kruskal-Wallis one-way ANOVA. Boxplots represent the median, 25th, and 75th percentiles, and whiskers represent measurements to the 5th and 95th percentiles. PC, principal component; PMI, post-mortem interval; Cntl, control; AsymAD, asymptomatic Alzheimer's disease; AD, Alzheimer's disease.



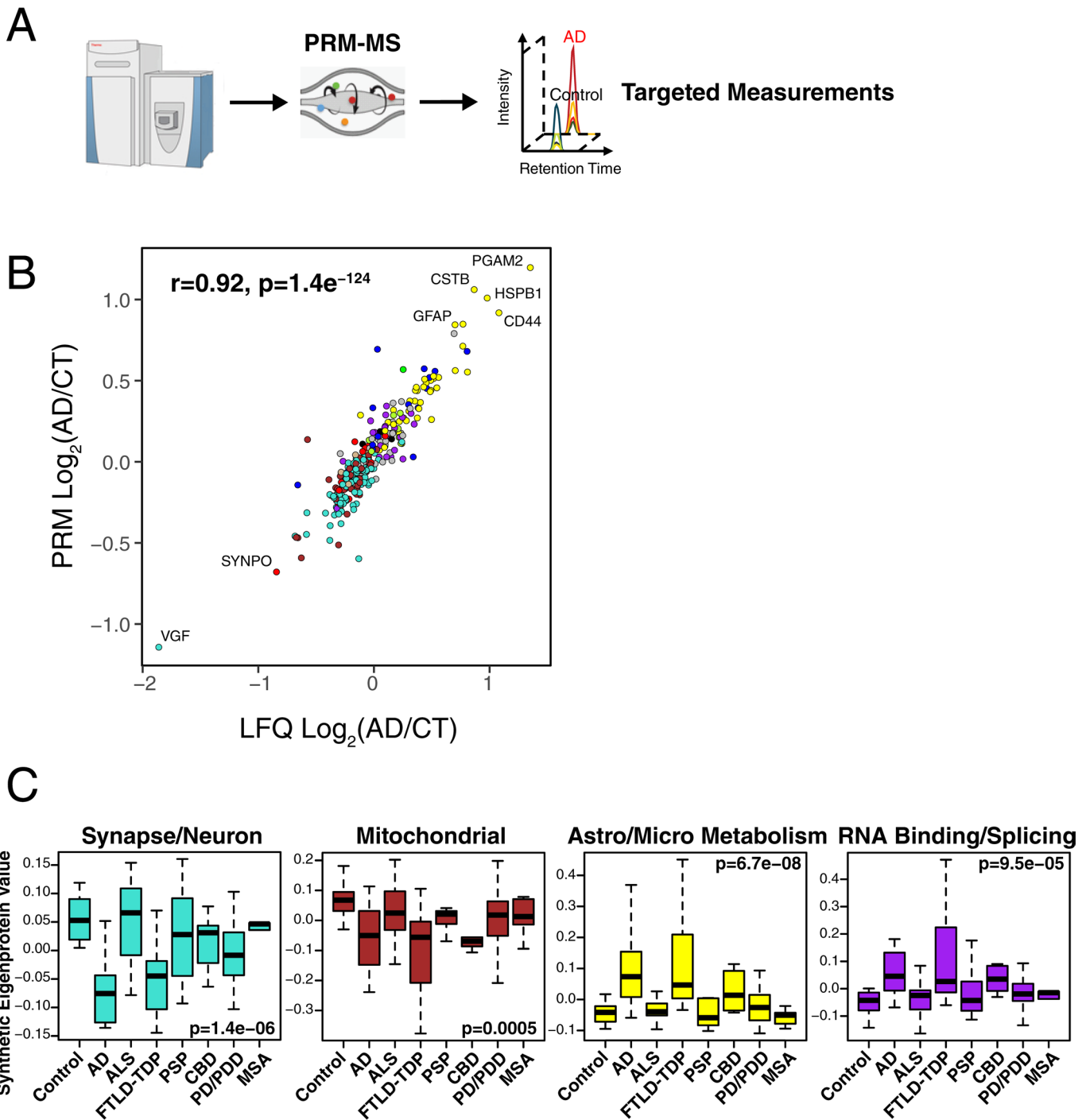
Extended Data Fig. 3 | Relationship of AD Network Proteins by t-SNE Analysis. Dimensionality reduction and visualization by t-distributed stochastic neighbor embedding (t-SNE) was applied to proteins that were in the top 25% by kME value within each AD network module. Proteins are color coded as shown in Fig. 1b according to the network module in which they reside. Network module ontologies and cell type enrichments are provided as shown in Fig. 1b. Ontologies are highlighted based on the most robust AD trait correlations as shown in Fig. 1b.



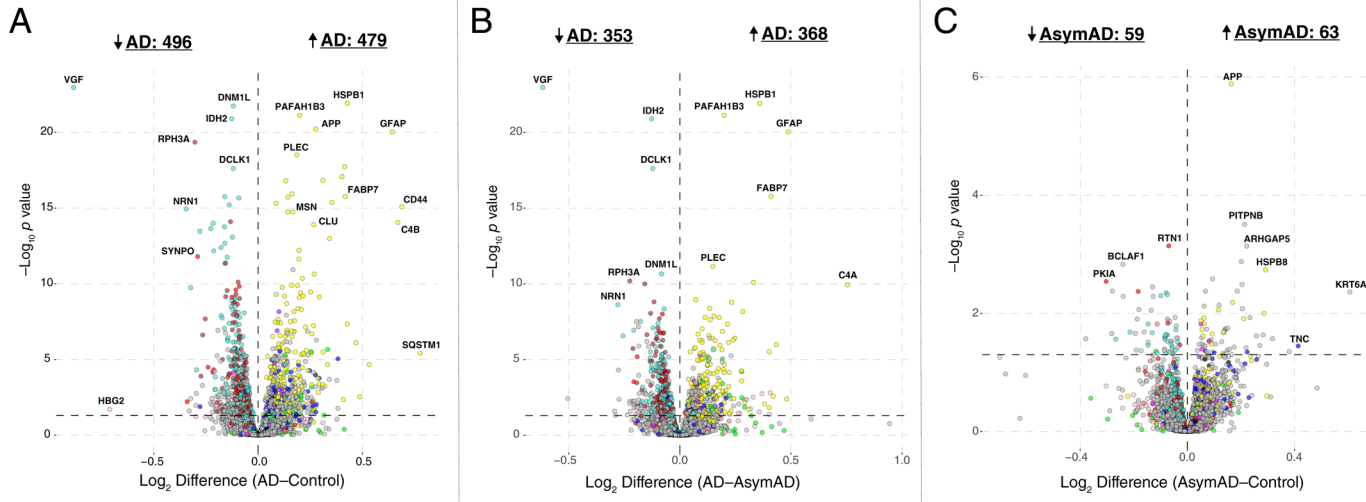
Extended Data Fig. 4 | AD Protein Network Module Trait and Pathology Correlations. **a–c**, The eigenprotein of each protein network module was correlated with neuropathological, molecular, and cognitive/functional traits ($n=419$ independent case sample traits after network connectivity outlier removal except for cognitive measures, where $n=167$ MMSE, $n=159$ CDR, and $n=56$ CASI) (a). Protein modules are bolded as in Fig. 1b using CERAD, Braak, MMSE, and CDR correlations. Strength of positive (red) or negative (blue) correlation is shown by two-color heatmap, with p values provided for all correlations with $p < 0.05$. (b), Correlation between CERAD plaque score and A β levels measured by label free quantification (LFQ) mass spectrometry¹⁷. (c), Correlation between Braak score (NFT, neurofibrillary tangle) and tau levels measured by LFQ of the microtubule binding region (MTBR). Correlations were performed using biweight midcorrelation and corrected by the Benjamini-Hochberg method. CERAD, Consortium to Establish a Registry for Alzheimer's disease A β plaque score (higher scores represent greater plaque burden); Braak, tau neurofibrillary tangle staging score (higher scores represent greater extent of tangle burden); A β , amyloid- β ; α -Syn, alpha synuclein; TDP-43, TAR DNA-binding protein 43; MMSE, mini-mental status examination score (higher scores represent better cognitive function); CDR, clinical dementia rating score (higher scores representing worse functional status); CASI, Cognitive Abilities Screening Instrument (higher scores represent better cognitive function). MMSE is from Banner, CDR is from MSSB, and CASI is from ACT.



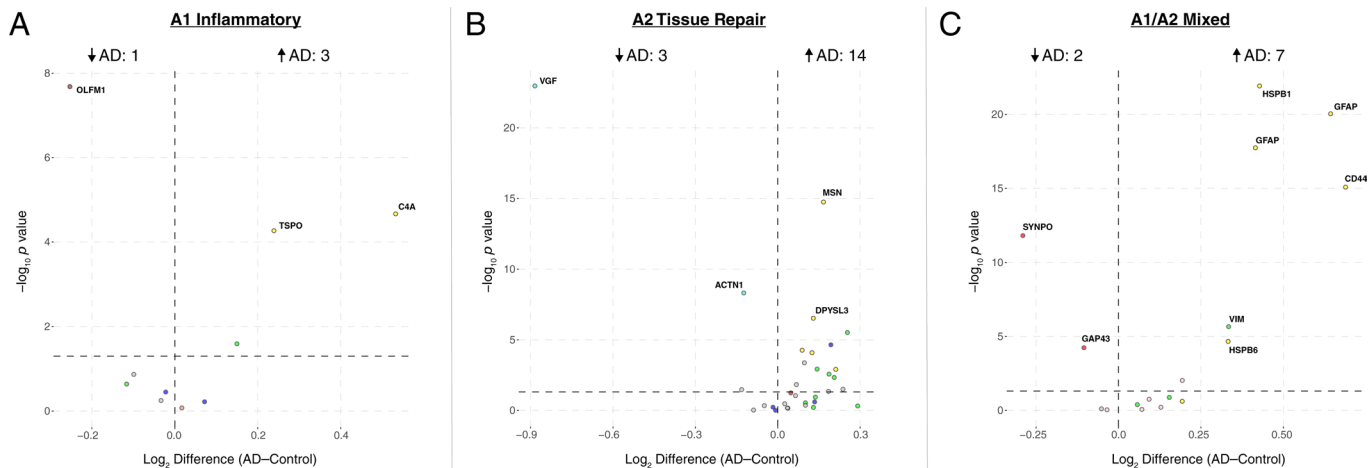
Extended Data Fig. 5 | AD Protein Network Validation in a Longitudinal Cohort of Aging. (a-c), Preservation of AD protein network modules and trait correlations in the Religious Orders Study and Memory and Aging Project (ROS/MAP) cohorts. (a), Protein levels from dorsolateral prefrontal cortex (DLPFC) in a total of 340 control, AsymAD, and AD cases (control, $n=84$; AsymAD, $n=148$; AD, $n=108$) from the ROS/MAP cohorts were measured using a different mass spectrometry platform and quantification approach compared to the cases used to generate the AD network as shown in Fig. 1. The resulting data were used to assess conservation of the AD brain protein network in the ROS/MAP cohorts. (b), AD brain protein network module preservation was calculated using a composite z_{summary} score as described by Langfelder et al.⁷⁴ The dashed blue line indicates a z_{summary} score of 1.96, or FDR q value <0.05 , above which module preservation was considered statistically significant. The dashed red line indicates a z_{summary} score of 10, or FDR q value $\sim 1e^{-23}$, above which module preservation was considered highly statistically significant. (c) Case status and trait preservation in the ROS/MAP cohorts. The top 20% of proteins by kME value in each AD brain protein network module was used to create a synthetic eigenprotein, which was then measured by case status in ROS/MAP and correlated with amyloid plaque load (CERAD score), tau neurofibrillary tangle burden (Braak stage), and cognitive function (global cognitive function composite z score). Synthetic eigenprotein analyses for modules M1, M3, M4, and M10 are shown. Analyses for all modules, with additional trait correlations, are provided in Supplementary Fig. 4. Differences in module synthetic eigenproteins by case status were assessed by Kruskal-Wallis one-way ANOVA. Module synthetic eigenprotein correlations were performed using biweight midcorrelation with Benjamini-Hochberg correction. Boxplots represent the median, 25th, and 75th percentiles, and whiskers represent measurements to the 5th and 95th percentiles. Cntl, control; AsymAD, asymptomatic Alzheimer's disease; AD, Alzheimer's disease.



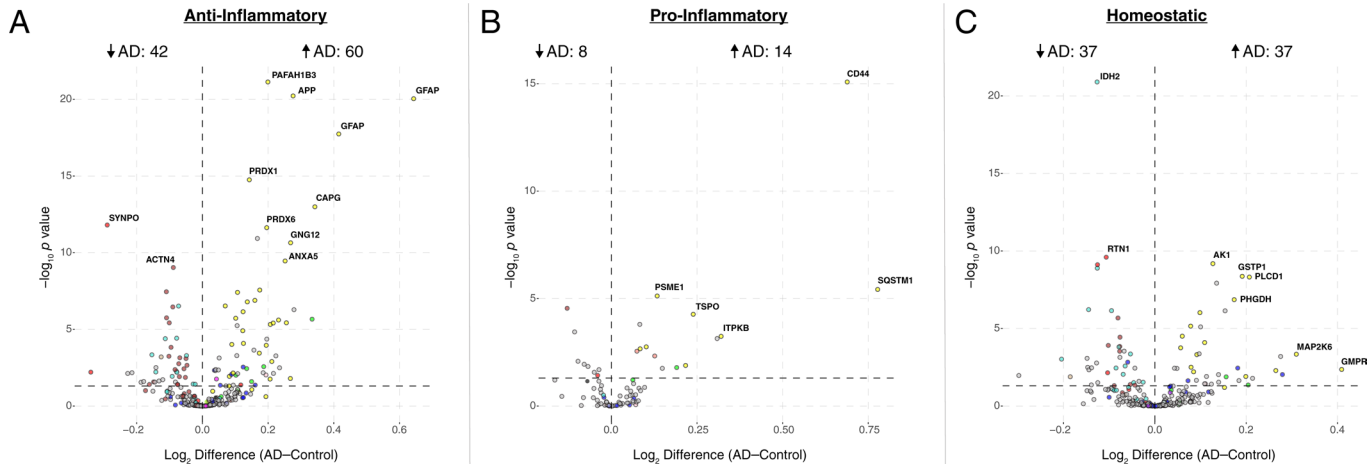
Extended Data Fig. 6 | AD Protein Network Module Changes in Other Neurodegenerative Diseases by PRM Analysis. **a-c**, Protein levels for 323 proteins across 108 brains from the UPenn cohort were measured by parallel reaction monitoring targeted mass spectrometry (PRM-MS) (**a**). Targeted peptides and individual protein measurements by disease group are provided in Supplementary Table 4 and Supplementary Fig. 11, respectively. (**b**), Protein levels across all cases were highly correlated between LFQ and PRM measurements ($n=307$ paired protein measurements). Correlation was performed by Pearson's rho and Student's significance (p). (**c**), A synthetic eigenprotein was created from proteins that mapped to an AD network module and measured across the different disease groups (control samples $n=46$, AD $n=49$, ALS $n=59$, FTLD-TDP $n=29$, PSP $n=27$, CBD $n=17$, PD/PDD $n=80$, and MSA $n=23$ after network connectivity outlier removal). Analyses for all modules are provided in Supplementary Fig. 12. Differences in module synthetic eigenproteins were assessed by Kruskal-Wallis one-way ANOVA. Differences between AD and other case groups were assessed by two-sided Dunnett's test, the results of which are provided in Supplementary Table 4. Boxplots represent the median, 25th, and 75th percentiles, and whiskers represent measurements to the 5th and 95th percentiles.



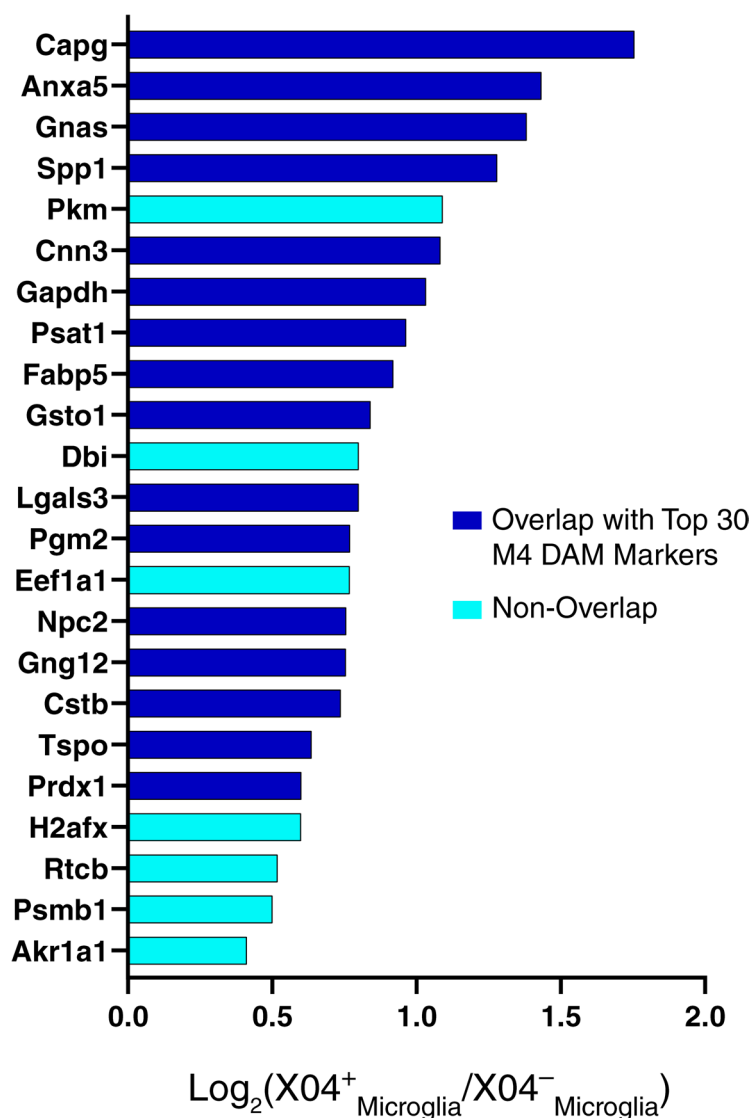
Extended Data Fig. 7 | Protein Differential Abundance in AD Brain. **a–c**, Differential protein abundance for AD versus control (**a**), AD versus AsymAD (**b**), and AsymAD versus control (**c**) brain, represented by fold-change versus *t* statistic for the given comparison ($n=230$ AD, $n=98$ AsymAD, $n=91$ control samples after network connectivity outlier removal). Differential abundance data are from the consensus analysis described in Fig. 1a. Proteins are colored by the module in which they reside according to the scheme shown in Fig. 1b. For instance, proteins that reside in module M4 are colored yellow. Pairwise comparisons were performed using one-way ANOVA with Tukey test. The bold horizontal dashed line represents $p < 0.05$. AsymAD, asymptomatic Alzheimer's disease; AD, Alzheimer's disease.



Extended Data Fig. 8 | Differential Abundance of Reactive Astrocyte Protein Markers in AD Brain. **a-c**, Proteins expressed in different astrocytic response states to acute injury²⁶ were analyzed for changes in AD. Astrocyte mRNAs that were upregulated greater than four-fold after acute injury by LPS administration (“A1” Inflammatory) (**a**), middle cerebral artery occlusion (“A2” Tissue Repair) (**b**), or both (“A1/A2 Mixed”) (**c**) were analyzed for changes in abundance between AD and control. Results are shown as protein fold-change versus *t* statistic for the given comparison ($n=230$ AD, $n=98$ AsymAD, $n=91$ control samples after network connectivity outlier removal). Pairwise comparisons were performed using one-way ANOVA with Tukey test. The bold horizontal dashed line represents $p < 0.05$. Proteins are colored by the module in which they reside according to the scheme shown in Fig. 1b. AD, Alzheimer’s disease.



Extended Data Fig. 9 | Differential Abundance of Microglial Phenotypic Protein Markers in AD Brain. **a–c**, Proteins corresponding to microglial mRNAs that were found to be associated with different microglial phenotypic states²⁷ were analyzed for changes in AD. Proteins from microglial co-expression modules corresponding to a disease-associated anti-inflammatory (**a**), disease-associated pro-inflammatory (**b**), and homeostatic (**c**) response phenotype were analyzed for changes in abundance between AD and control. Results are shown as protein fold-change versus t statistic for the given comparison ($n=230$ AD, $n=98$ AsymAD, $n=91$ control samples after network connectivity outlier removal). Pairwise comparisons were performed using one-way ANOVA with Tukey test. The bold horizontal dashed line represents $p < 0.05$. Proteins are colored by the module in which they reside according to the scheme shown in Fig. 1b. AD, Alzheimer's disease.



Extended Data Fig. 10 | M4 Astrocyte/Microglial Metabolism Module Members Increased at the Transcript Level in Microglia Undergoing Active Amyloid-β Plaque Phagocytosis. mRNA transcripts increased in microglia undergoing active amyloid-β plaque phagocytosis (XO4^+)³³ were overlapped with cognate proteins in the M4 module. There were 23 transcripts that overlapped with M4 module members. Proteins that also overlapped with the top 30 disease-associated microglia (DAM) markers in the M4 module (Fig. 5d) are shown in blue. Proteins that did not overlap with the top 30 DAM markers are shown in cyan. Proteins in cyan are therefore M4 members that may be more specifically elevated in microglia undergoing active amyloid-β plaque phagocytosis.

Reporting Summary

Nature Research wishes to improve the reproducibility of the work that we publish. This form provides structure for consistency and transparency in reporting. For further information on Nature Research policies, see [Authors & Referees](#) and the [Editorial Policy Checklist](#).

Statistics

For all statistical analyses, confirm that the following items are present in the figure legend, table legend, main text, or Methods section.

n/a Confirmed

- The exact sample size (n) for each experimental group/condition, given as a discrete number and unit of measurement
- A statement on whether measurements were taken from distinct samples or whether the same sample was measured repeatedly
- The statistical test(s) used AND whether they are one- or two-sided
Only common tests should be described solely by name; describe more complex techniques in the Methods section.
- A description of all covariates tested
- A description of any assumptions or corrections, such as tests of normality and adjustment for multiple comparisons
- A full description of the statistical parameters including central tendency (e.g. means) or other basic estimates (e.g. regression coefficient) AND variation (e.g. standard deviation) or associated estimates of uncertainty (e.g. confidence intervals)
- For null hypothesis testing, the test statistic (e.g. F , t , r) with confidence intervals, effect sizes, degrees of freedom and P value noted
Give P values as exact values whenever suitable.
- For Bayesian analysis, information on the choice of priors and Markov chain Monte Carlo settings
- For hierarchical and complex designs, identification of the appropriate level for tests and full reporting of outcomes
- Estimates of effect sizes (e.g. Cohen's d , Pearson's r), indicating how they were calculated

Our web collection on [statistics for biologists](#) contains articles on many of the points above.

Software and code

Policy information about [availability of computer code](#)

Data collection

MaxQuant v1.6.3.4 with Thermo Foundation 2.0 for RAW file reading capability, Proteome Discoverer Suite (v2.3)

Data analysis

Skyline (v4.2), TAMPOR batch correction v0.75 (<https://github.com/edammer/TAMPOR>), Oldham's 'SampleNetworks' v1.06 R script for network connectivity outlier removal, Weighted Correlation Network Analysis (WGCNA) algorithm, GO Elite v1.2.5, MAGMA, R (v3.5.2), R package Rtsne, R package igraph

For manuscripts utilizing custom algorithms or software that are central to the research but not yet described in published literature, software must be made available to editors/reviewers. We strongly encourage code deposition in a community repository (e.g. GitHub). See the Nature Research [guidelines for submitting code & software](#) for further information.

Data

Policy information about [availability of data](#)

All manuscripts must include a [data availability statement](#). This statement should provide the following information, where applicable:

- Accession codes, unique identifiers, or web links for publicly available datasets
- A list of figures that have associated raw data
- A description of any restrictions on data availability

All data are publicly available at <https://www.synapse.org/consensus>. ROSMAP resources can be requested at www.radc.rush.edu.

Field-specific reporting

Please select the one below that is the best fit for your research. If you are not sure, read the appropriate sections before making your selection.

- Life sciences Behavioural & social sciences Ecological, evolutionary & environmental sciences

For a reference copy of the document with all sections, see nature.com/documents/nr-reporting-summary-flat.pdf

Life sciences study design

All studies must disclose on these points even when the disclosure is negative.

Sample size	No sample size calculation was performed. Sample size was chosen based on the available data. The recommended number of samples to include in correlation network analysis to reduce the chance of spurious correlation is n=20-30 (Oldham, Transcriptomics: from differential expression to coexpression, 2014). This study included n=419 samples after network outlier removal, and was therefore well powered to avoid spurious correlations. It was also powered to detect weak module eigenprotein trait correlations at a bicor rho value of ~0.1.
Data exclusions	We used pre-established criteria to define control, AsymAD, and AD cases in each cohort prior to analysis. See Methods for further details and references. Network outlier removal was performed uniformly and consistently across cohorts using Oldham's 'SampleNetworks' v1.06 R script with a 3 fold-SD cutoff of Z-transformed sample connectivity, which is a customary threshold used for connectivity outlier removal. Removing connectivity outliers greatly improves the quality of the network by lowering the scale free topology power necessary to reach criteria for approximate scale-free properties of the calculated correlation network, which in turn appropriately downweights outlier protein measurements from overtly impacting the network structure.
Replication	The consensus network was replicated in the ROSMAP cohort. All network modules were preserved in ROSMAP. CSF biomarkers were also validated in a replication cohort. Most markers could be replicated. All discovery and replication data are provided.
Randomization	For each cohort, samples were randomized prior to mass spectrometry-based proteomic analysis based on available traits.
Blinding	Blinding was not relevant to this study because intervention bias was not an issue given the nature of the study

Reporting for specific materials, systems and methods

We require information from authors about some types of materials, experimental systems and methods used in many studies. Here, indicate whether each material, system or method listed is relevant to your study. If you are not sure if a list item applies to your research, read the appropriate section before selecting a response.

Materials & experimental systems		Methods	
n/a	Involved in the study	n/a	Involved in the study
<input checked="" type="checkbox"/>	<input type="checkbox"/> Antibodies	<input checked="" type="checkbox"/>	<input type="checkbox"/> ChIP-seq
<input checked="" type="checkbox"/>	<input type="checkbox"/> Eukaryotic cell lines	<input checked="" type="checkbox"/>	<input type="checkbox"/> Flow cytometry
<input checked="" type="checkbox"/>	<input type="checkbox"/> Palaeontology	<input checked="" type="checkbox"/>	<input type="checkbox"/> MRI-based neuroimaging
<input checked="" type="checkbox"/>	<input type="checkbox"/> Animals and other organisms		
<input type="checkbox"/>	<input checked="" type="checkbox"/> Human research participants		
<input checked="" type="checkbox"/>	<input type="checkbox"/> Clinical data		

Human research participants

Policy information about [studies involving human research participants](#)

Population characteristics	CSF Cohort 1 = 150 AD, 70/80 (M/F), Avg Age 68; 147 Control, 41/106 (M/F), Avg Age 65 CSF Cohort 2 = 33 AD, 16/17 (M/F), Avg Age 73; 31 AsymAD, 12/19 (M/F), Avg Age 64; 32 Control, 14/18 (M/F), Avg Age 63
Recruitment	Participants who provided CSF were recruited from the cognitive neurology clinic at Emory, the Emory Alzheimer's Disease Research Center, and the community through various outreach efforts. Symptomatic AD individuals were recruited from a clinical neurology practice that exclusively focuses on Alzheimer's disease and related disorders in an academic referral center and may not be representative of patients in general clinical practice. Healthy control volunteers are subject to self-selection bias and are typically healthier and better educated than the general population. Because of the Alzheimer's disease focus of the research studies through which they were recruited, there is likely to be an over-representation of individuals with a family history of Alzheimer's disease.
Ethics oversight	All participants from whom CSF samples were collected provided informed consent under protocols approved by the Institutional Review Board (IRB) at Emory University

Note that full information on the approval of the study protocol must also be provided in the manuscript.